Optimal Therapy Design With Tumor Microenvironment Normalization[3]

Chenyu Wang[1] | Samuel Degnan-Morgenstern[1] | John D. Martin[2*] | Matthew D. Stuber[1*]

[1]Process Systems and Operations Research Laboratory, Department of Chemical and Biomolecular Engineering, University of Connecticut, Storrs, CT, 06269-3222, USA

[2]Materia Therapeutics, Las Vegas, NV, 89158, USA

Correspondence
Matthew D. Stuber, University of Connecticut, Storrs, CT, 06269-3222, USA
John D. Martin, Materia Therapeutics Inc., Las Vegas, NV, 89158, USA
Email: stuber@alum.mit.edu (MDS); jdmartin@alum.mit.edu (JDM)

Tumor microenvironment (TME) normalization improves efficacy by increasing anticancer nanocarrier delivery by restoring transvascular pressure gradients that induce convection. However, transport depends on TME biophysics, normalization dose, and nanocarrier size. With increased understanding, we could use computation to personalize normalization amount and nanocarrier size. Here, we use deterministic global dynamic optimization with novel bounding routines to validate mechanistic models against in vivo data. We find that normalization with dexamethasone increases the maximum transvascular convection rate of nanocarriers by 48-fold, the tumor volume fraction with convection by 61%, and the total amount of convection by 360%. Nonetheless, 22% of the tumor still lacks convection. These findings underscore both the effectiveness and limits of normalization. Using artificial neural network surrogate modeling, we demonstrate the feasibility of rapidly determining the dexamethasone dose and nanocarrier size to maximize accumulation. Thus, this digital testbed quantifies transport and performs therapy design.

---

*Co-corresponding authors.

---

1 | INTRODUCTION

Solid tumors feature pathophysiological abnormalities that are biophysical barriers to the transport of anticancer drugs. These barriers impede the effectiveness of such therapies by limiting their accumulation and spatial distribution [1]. Ameliorating the pathophysiology such that tumor microenvironment (TME) components have a more "normalized" phenotype increases small-molecule and nanocarrier-based therapies' delivery and efficacy in cancer patients [2,3,4]. However, TME normalization combined with anticancer therapies has yet to lead to cures throughout a cancer patient population. Thus, a deeper understanding of how TME normalization affects the transport of therapies within tumors is necessary to fully bypass these spatially and temporally heterogeneous biophysical barriers. Mathematical modeling can be used to construct a robust framework for studying how the normalized TME modulates biophysical barriers to transport phenomena in tumors, thereby enabling the discovery of deeper insights into effective TME normalization. In turn, such a framework may serve as the foundation for establishing a technology platform for effective therapy design to improving therapeutic efficacy.

1.1 | Cancer Biology

Nanoscale anticancer therapies on the order of dozens of nanometers, including macromolecules such as polymeric micelles and antibodies, benefit from longer systemic circulation due to slower clearance, selective accumulation in tumors due to leaky tumor blood vessels, and long retention in tumor tissue due to dense fibrosis and non-functional lymphatics in the TME [1]. In fact, nanoscale therapies are currently in use today with cancer patients [3]. Nonetheless, leaky blood vessels, dense fibrosis, and nonfunctional lymphatics collaborate to construct biophysical barriers that reduce the effectiveness of cancer treatments [1,3,4,5]. Nanoscale therapies are affected in a size-dependent manner [6,7]. In tumors, plasma from circulation excessively extravasates from leaky blood vessels to the interstitial (i.e. extravascular) space, yet moves slowly because dense fibrosis limits fluid movement [8]. Ultimately, fluid cannot be cleared because tumor lymphatics are non-functional [9]. Thus, one distinguishing feature of tumors is an elevated interstitial fluid pressure (IFP), that eliminates transvascular convective transport of drugs in tumors by reducing the transvascular pressure gradient to zero [1,8].

Vascular normalization involves fortifying leaky tumor blood vessels by blocking angiogenesis [2,10]. ECM normalization involves reversing dense fibrosis by reprogramming cancer-associated fibroblasts to a quiescent phenotype so that the fibroblasts stop producing and maintaining excessive levels of extracellular matrix (ECM) [2,10,11]. As a result, the dense fibrosis, which slows interstitial fluid movement and compresses intratumor lymphatic tumor vessels such that they are nonfunctional [12], is diminished. Already, vascular normalization is used with nanomedicine in patients [13], while ECM normalization recently succeeded in a clinical trial with small-molecule chemotherapy [14].

We recently discovered that dexamethasone, which is a glucocorticoid steroid often used to manage chemotherapy-related toxicities, can induce vascular and ECM normalization simultaneously if used at an appropriate dose and schedule [10]. Yet, how dexamethasone affects blood vessel leakiness, fibrosis, and lymphatic vessel function towards alleviating IFP and restoring a transvascular pressure gradient is multi-factored. Each factor depends on the dose of

dexamethasone differently. Furthermore, how the size of nanocarrier-based anticancer drugs interacts with these factors is unclear. Therefore, enhancing the delivery of nanocarriers is a multi-faceted engineering problem, so a model-based systems engineering approach is required to better understand the underlying physical phenomena and complex relationships of the biological system. Throughout this work, we will use the term *nanocarrier* to include nanoscale therapies, in general.

1.2 | Modeling and Simulation for Cancer

Transport of nanocarriers from the systemic circulation to cancer cells includes three steps: flow through blood vessels to different regions of the tumor, transvascular transport, and transport through the interstitial space of the tumor. Specifically, the capillary vasculature is a highly dynamic region for transvascular transport of medicine, nutrients, and waste materials being exchanged between the blood vessels and the interstitial space. There are two key transvascular transport mechanisms: diffusion and convection. Generally, smaller nanocarriers benefit from diffusion using concentration gradients as an additional driving force for transvascular transport, whereas larger nanocarriers must rely on convective transport using pressure gradients due to steric hindrances that make diffusion very slow [1,15]. Previous studies have indicated that diffusion is the main mechanism of mass transport across the vessel wall in tumors, because of the lack of transvascular pressure gradients [1,9]. However, dexamethasone affects blood vessel leakiness, fibrosis, and lymphatic function, so it could restore transvascular pressure gradients. How diffusion and convection are affected for differently sized nanocarriers is unclear. To investigate, a first-principles-based modeling approach is required to quantify the important physiological parameters that govern transport in tumors.

The vascular and interstitial transport phenomena in tumors have been extensively modeled. Baxter and Jain [16,17,18,19] developed a one-dimensional spherical tumor model that describes fluid and nanocarrier transport and accounts for transvascular transport through pores. [20,21] Baish et al. [22] developed a two-dimensional fluid transport model that considered coupling between the vessels and the interstitial space of tumors in a unified theoretical framework. Subsequently, Chauhan et al. [7] applied this coupled transport system to a percolation-based tumor vasculature network and subsequently established the solute transport model on this network. Sweeney et al. [23] further developed a three-dimensional model to simulate vascular blood flow and interstitial fluid transport. Their model integrated the complex vascular structure to provide a visualization of spatial heterogeneity, which can predict the response of fluid dynamics following vascular normalization therapy. Through simulation of vascular normalization, the authors concluded that therapies should "seek to develop an IFP gradient," which is consistent with the overall simulation results and conclusions of previous computational studies of tumor vascular normalization.

In addition to first-principles mechanistic models, artificial intelligence (AI) has been gradually becoming a popular model-based approach in pharmacokinetics/ pharmacodynamics (PKPD) studies [24,25,26]. An efficient machine learning model simplifies computationally intensive simulations by creating mathematically simple regression models that capture input-output relationships with high accuracy [27]. Specifically, artificial neural networks (ANNs) are powerful computational models that are capable of approximating and predicting the behavior of such complicated systems with high accuracy and efficiency [28].

In this work, we establish a systematic *in silico* model-based framework using deterministic global optimization for optimal therapy design within the context of TME-normalization processes. First, we propose using deterministic global optimization to solve the parameter estimation problems and provide a rigorous quantitative foundation for *in silico* model discrimination. Using this foundation, we quantify the relative contributions of convection and diffusion to solute transport across the vessel walls. Moreover, we develop an optimal TME-normalizing therapy design approach for dose selection that demonstrates the relationship between dexamethasone dose and the interstitial concentra-

tion of anticancer drugs in the pharmacokinetic system. Finally, we use this tumor transport model to determine an optimal nanomedicine size for the greatest accumulation in the tumor interstitial space. We also propose an ANN surrogate modeling approach to reduce the computational cost of solving challenging deterministic global optimization problems for model validation, dexamethasone dose selection, and anticancer nanocarrier size selection. The details of establishing and using such machine learning models within optimization-based decision-making frameworks are presented in this work.

Our work seeks to enhance the practicability and predictive capabilities of tumor transport models using mechanistic and data-driven model validation approaches and rigorous methods in global optimization for stronger model-based systems engineering approaches for optimal therapy design in cancer research. The information obtained through this approach aids in the development of better models and provides deeper insight into the physical behavior of molecular transport during TME normalization to guide drug development and delivery.

2 | METHODS

Figure 1 illustrates the overall systematical framework proposed for model-based TME-normalizing therapy and drug size design. To enhance the predictive capabilities of the models and provide confidence in their utility for the model-based approach for drug and therapy development, we propose to use formal methods to estimate and quantify the critical parameters for model validation. This approach requires solving a nonconvex nonlinear program (NLP) constrained by the mechanistic tumor transport model as an unsteady partial differential equation (PDE). A simulation-based feasible path approach is proposed and the PDE-constrained optimization problem is reformulated as a box-constrained NLP. In addition, ANN machine learning methods are proposed to construct surrogate models for reducing the time costs of solving global optimization problems. Moreover, the well-established mechanistic and ANN models are also used in TME-normalizing therapy design for optimal neoadjuvant dose selection as well as drug size design for anticancer nanocarriers.

2.1 | Parameter Estimation and Model Validation by Deterministic Global Optimization

The glucocorticoid steroid DEX, an agent mainly used for alleviating chemotherapy side effects, has been identified as a pre-treatment adjunct agent for normalizing metastatic tumor vessels and ECM for enhanced efficacy of drug delivery[10]. To verify the effects of DEX on nanocarrier delivery through vascular and ECM normalization processes, we propose to determine the optimal solutions of the parameter estimation problems introduced in Martin et al.[10] by deterministic global optimization. This approach is significant because only global optimal solutions can guarantee the most accurate fit to the obtained experimental data. The mechanistic tumor transport model used in this work is introduced in the Supplementary Information (SI).

Martin et al.[10] conducted a series of experiments *in vivo* to investigate the efficacy of DEX. In these experiments, immunocompetent mice bearing orthotopic 4T1 breast cancer were treated with 3 and 30 mg/kg DEX daily for 4 days. After which, two types of fluorescent dyes (70 kDa rhodamine-bound dextran and 500 kDa FITC-bound dextran) were injected as tracers[10]. *In vivo* confocal laser scanning microscopy was employed to characterize the spatiotemporal distribution of dextrans in mouse tumors treated with different doses of DEX[6]. Based on the intravital microsopy images, the effective permeability P_{eff} was quantified as the rate of nanoparticle fluorescent signal passing through the vessel walls normalized to the vessel surface area and the transvascular concentration difference[7]. Note that the effective permeability includes both convective and diffusive components; however, it significantly overestimates the
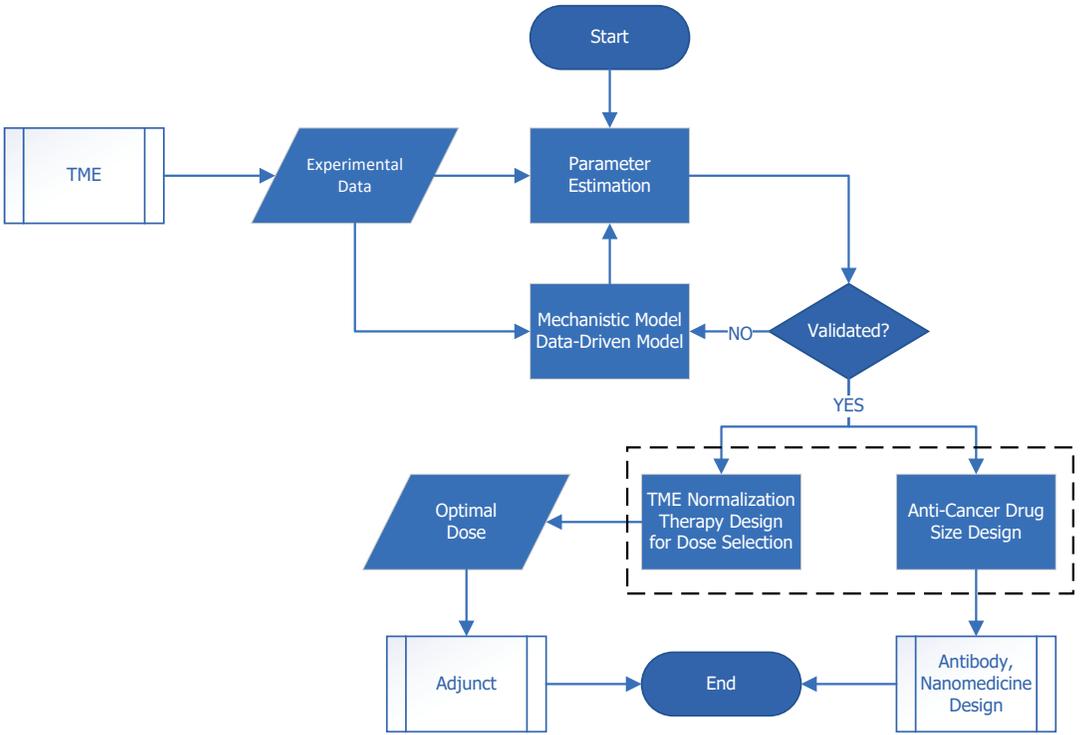
FIGURE 1 A flowchart is illustrated demonstrating a systematical framework for optimal therapy design within the context of tumor microenvironment (TME) normalization. Based on the experimental data, parameter estimation is utilized to validate/invalidate a proposed mechanistic model or data-driven model of the tumor. Validated models are then applied to tumor TME normalization therapy design for dose selection and anticancer drug size design. Note that the TME normalization therapy design and drug size design in the dashed line box can be implemented separately, sequentially or simultaneously.

diffusive part and may not be consistent with actual transcapillary transport[16]. Then, the spatial average concentration of the interstitial space was calculated from the conservation equation[7]:

$$\frac{dc_{\text{avg}}^{\text{data}}}{dt} = P_{eff} \frac{S}{V} \left(c_v - c_{\text{avg}}^{\text{data}} \right),$$

where c_v is the solute concentration in the vessels of a tumor (g/mL) and $\frac{S}{V}$ is the vascular surface area per unit volume (cm^{-1}). This serves as an experimental concentration profile for subsequent parameter estimation problems used for elucidating the physiological effects of DEX treatment.

In this work, a similar approach is taken whereby the dimensionless spatially-averaged concentration of solute $\hat{c}_{\text{avg}}^{\text{data}}$ (determined from the overall conservation equation) serves as an experimental concentration profile for each P_{eff} measured experimentally and is used for parameter estimation of the mechanistic model of interest. Deterministic global optimization methods are used to validate the mechanistic model by finding the parameter values that result in the proposed model fitting the experimental data as best as possible, and subsequently verifying the TME-normalization process. The objective function is formulated as the sum-of-squared errors (SSE) between the average

concentration profile predicted by the model and the measured data (from the overall conservation expression with the experimentally measured P_{eff}) at discrete time points over the entire time horizon of the experiment. Inequality constraints are formulated for the IFP profiles based on experimentally determined values. The parameter estimation problem is formulated as:

$$\min_{\boldsymbol{\pi} \in \Pi} \sum_{i=1}^{n} \left(\hat{c}_{\text{avg}}(t_i, \boldsymbol{\pi}, d_m) - \hat{c}_{\text{avg}}^{\text{data}}(t_i) \right)^2 \tag{1}$$

$$\text{s.t. } \hat{p}_{peri}(\boldsymbol{\pi}) \leq \hat{p}_{peri,\max}$$

$$\hat{p}_{peri}(\boldsymbol{\pi}) \geq \hat{p}_{peri,\min},$$

where the dimensionless spatially-averaged concentration of solute $\hat{c}_{\text{avg}}$ is calculated by averaging the dimensionless concentration $\hat{c}$ for all spatial nodes (discretization details are introduced in Section 2.7 from the mechanistic solute transport model (details are introduced in the SI) and taken as the parametric model output for the parameter estimation problem. The decision variables $\boldsymbol{\pi} = (L_p, K) \in \Pi \subset \mathbb{R}^{n_\pi}$ is the vector of physiological parameters of the model to be estimated, with L_p the hydraulic conductivity of the microvascular wall (cm/mm Hg-sec) and K the hydraulic conductivity of tumor interstitium (cm^2/mm Hg-sec). The parameter d_m is the diameter of the nanocarrier (nm) used in the corresponding experiment. The SSE objective fits the model-predicted profile to the experimental profile at each time node t_i selected within the time horizon (5 min), with $i \in \{1, \ldots, n\}$. For the inequality constraints, we introduce $\hat{p}_{peri}$ as the dimensionless superficial (peripheral) IFP, which is calculated by the dimensionless IFP $\hat{p}$ in the superficial region (introduced in Section 2.7, and $\hat{p}_{peri,\max}$ and $\hat{p}_{peri,\min}$ as the physical bounds of $\hat{p}_{peri}$, with values taken from Martin et al. [10] and listed in Table 1.

TABLE 1 The physical bounds on the superficial (peripheral) tumor IFP for the control, 3 mg/kg, and 30 mg/kg DEX treatment case are reported here as determined by Martin et al. [10]. These values are used in the parameter estimation problems formulated as (1) to ensure that physically meaningful solutions are identified.

Dose	Control	3 mg/kg	30 mg/kg
$\hat{p}_{peri,\min}$ (mmHg)	4.87	3.02	1.95
$\hat{p}_{peri,\max}$ (mmHg)	5.67	3.62	2.45

2.2 | Bounding Methods for Tumor Transport Model

Deterministic global optimization can prevent erroneously invalidating mechanistic models in cases where suboptimal solutions obtained by local optimization algorithms result in poor fits. Methods for solving global optimization problems in this work rely on the branch-and-bound (B&B) framework [29] for deterministic search. Specifically, we employ the flexible and open-source B&B-based solver EAGO [30,31]. The B&B algorithm iteratively partitions the search space into successively smaller subdomains and solves a sequence of lower- and upper-bounding subproblems on each subdomain. The algorithm converges in finitely-many iterations to an ϵ-optimal global solution or terminates with a certificate of infeasibility by comparing the obtained bounds across nodes. The upper-bounding problems typically determine a feasible local solution (if one exists) on each subdomain. The lower-bounding problems rely on the ability to calculate rigorous global bounds on all variables and functions involved in the optimization formulation. Calculating valid lower bounds for a global optimization problem is the most challenging procedure. This is especially true for PDE

systems encountered in this work, as this task amounts to constructing rigorous bounds on the spatiotemporal state solutions over the entire domain of optimization variables (i.e., the reachable set).

In this section, we present a method for constructing global bounds enclosing the reachable sets of the tumor transport model. Several different bounding methods are presented and analyzed in this work to determine the most effective method for use with the tumor transport model. The fundamental approach is to use the method of lines with finite differences for spatial discretization and then differential inequalities (DI)[32,33] to construct state bounds of the discretized large-scale ODE-IVP system. Note that apart from implementing interval arithmetic[34] (IA) for constructing bounds, a mixed interval arithmetic/affine arithmetic[35,36] (IA/AA) approach was also implemented[37]. In addition to standard DI, a modified DI approach with interval refinement operators[38] was also implemented for problems with prescribed bounding information known *a priori*. An overview of these set-valued mapping approaches is introduced in Section S2 of the SI. In summary, four bounding methods are considered for comparison: IA and DI, IA and DI with interval refinement, IA/AA and DI, and IA/AA and DI with interval refinement.

Significant nonlinearity of the models poses a major challenge to efficiently constructing tight bounds. In the tumor transport model, a problematic term that requires special consideration is the solute source term that describes the transvascular mass transport of nanocarriers:

$$\phi_s = L_p \frac{S}{V} (p_v - p)(1 - \sigma) c_v + P \frac{S}{V} (c_v - c) \frac{Pe}{e^{Pe} - 1}. \tag{2}$$

Here, p_v is the vascular pressure (mm Hg), p is the interstitial fluid pressure (IFP) (mm Hg), σ is the solute reflection coefficient, P is the vascular permeability of the solute through the vascular wall (cm/sec), c is the solute concentration in the interstitial space of the tumor (g/mL), and $Pe = L_p (p_v - p)(1 - \sigma)/P$ is the Péclet number representing the ratio of the rates of convection to diffusion across the vascular wall.

The solute source term suffers from the *dependency problem* of IA (i.e., the overestimation of interval operations due to the same variables being treated independently). The nonlinearity caused by the exponential terms significantly magnifies this overestimation. We overcome the dependency problem using the following strategy. Since Pe appears both in the numerator and in the denominator of the term $\frac{Pe}{e^{Pe}-1}$ in (2), without special consideration, the dependency problem will lead to an appreciable overestimation of the bounds that will be detrimental to the B&B procedure. To avoid this, we consider the function $z(x) = \frac{x}{e^x - 1}$, where we seek a real interval $Z = [z^L, z^U]$ such that $z(x) \in Z$ for every $x \in [Pe^L, Pe^U]$, for known values Pe^L and Pe^U. It is easy to prove that z is a monotonically decreasing function of x, and therefore, the exact bounds on the range of z on the domain $[Pe^L, Pe^U]$, can be derived as:

$$z^L = \frac{Pe^U}{e^{Pe^U} - 1},$$
$$z^U = \frac{Pe^L}{e^{Pe^L} - 1}.$$

The definitions of these exact bounds are used throughout this work.

Bounds on the state variables of the tumor transport model were constructed based on four approaches. The spatial domain was discretized into $N = 100$ nodes and the discrete-time DI scheme[39] was used to construct the bounds through the simulation time (5 min) with 21 time steps. The two physiological parameters are considered as decision variables and bounded by an interval domain $\pi = (L_p, K) \in \Pi = [7.5 \times 10^{-7}, 7.6 \times 10^{-7}] \times [1.15 \times 10^{-6}, 1.2 \times 10^{-6}]$. The numerical solutions and bounding results are illustrated in Figure 2 for the four bounding methods considered.

To compare the effectiveness of the different bounding procedures, the volumes between the upper and lower
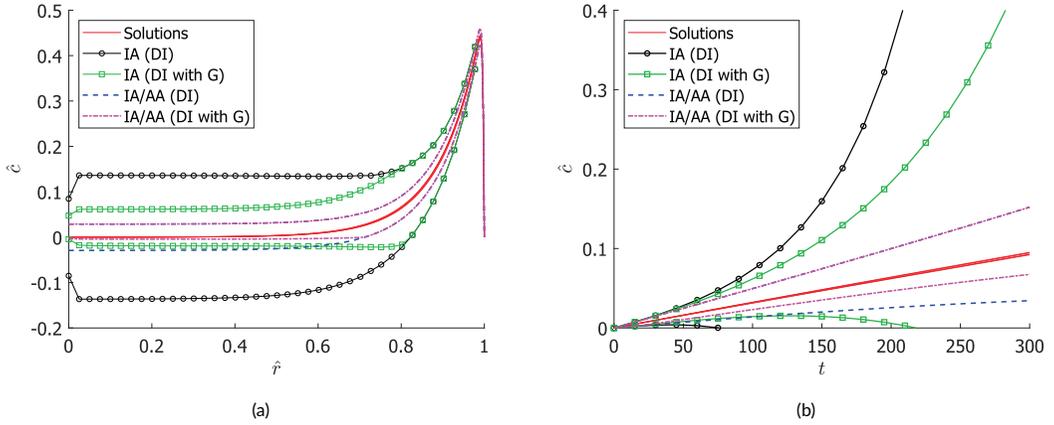
(a)   (b)

FIGURE 2   Numerical solutions and bounding results for the tumor transport model are plotted. (a) The spatial profiles of the dimensionless concentration $\hat{c}$ in the tumor at $t = 150$ s are plotted for several values of π along with the state bounds derived from pure IA, IA with modified DI, mixed IA/AA, and mixed IA/AA with modified DI. (b) The trajectories of the solute concentration $\hat{c}$ in the tumor at the position $\hat{r} = 0.5$ are plotted for several values of π along with the state bounds derived from pure IA, IA with modified DI, mixed IA/AA, and mixed IA/AA with modified DI. $\hat{c}$ is approximated by corresponding numerical solutions calculated by the explicit Euler method, and the state bounds are calculated by the discrete-time DI method.

bounds on the dimensionless concentration over the entire spatial and time domains are quantified along with the corresponding time costs for constructing these bounds, and listed in Table 2. It is observed that the time costs for pure IA and mixed IA/AA methods are almost the same, but the mixed IA/AA method can provide much tighter bounds. If taking the prescribed physical bounds $\hat{c} \in G = [0, 5]$ into account with the modified DI method, both pure IA and mixed IA/AA methods can enhance the bounding results. However, the increased computational costs are nearly two orders-of-magnitude more than standard DI due to the curse of the dimensionality of the discretized systems. The dramatic burden in time cost using the modified DI method overshadows any improvement of the bounding results in this case. As indicated by the volumes in Table 2, the bounds constructed by mixed IA/AA and standard DI methods are already relatively efficient (91.3 % tighter than the IA method, 62.4 % tighter than the IA (DI with G) method, and only 37.6 % larger than the IA/AA (DI with G) method), and the modified DI will not contribute much to reducing the conservatism. Therefore, in this study, we propose to use the mixed IA/AA and standard DI method as the bounding routine for solving all global optimization problems.

TABLE 2   The achieved volumes and time costs are reported for the different bounding methods considered in this study. The IA/AA bounds are significantly tighter than the pure IA bounds (91% reduction in volume) without additional computational time. The IA/AA bounds are also nearly as tight as the IA/AA (DI with G) bounds (38% increase in volume) but with almost two order-of-magnitude less computational time.

Bounding Methods	IA	IA/AA	IA (DI with G)	IA/AA (DI with G)
Volume	0.6438	0.0560	0.1489	0.0407
Time (s)	0.5342	0.5312	47.21	47.67

2.3 | Machine Learning Model

Machine learning regression is proposed to establish a computationally efficient artificial neural network (ANN) as a surrogate for the mechanistic tumor transport model. The established ANN models will then be used to solve the model validation parameter estimation problems as formulated in (1). This approach is proposed to analyze the relative performance and accuracy of ANN models to assess their applicability within the proposed framework for drug and therapy design, as well as broader contexts of scientific machine learning in cancer research and therapy. The work in this subsection was implemented in Julia[40] 1.6.1 running on an Intel Xeon W-2195 (18-core/32-thread) 2.3 GHz/4.3 GHz (base/turbo) CPU with 64GB RAM running Windows 10 Pro. The inputs for the ANNs considered are the two physiological parameters L_p and K, discussed previously. Since DEX treatment normalizes the TME and, in turn, affects the transport phenomena in tumors, different ANN surrogate models were constructed to represent the control and DEX treated tumors for greater accuracy. Furthermore, since the experimental data varied slightly across the 70 kDa nanocarrier and 500 kDa nanocarrier experimental groups, separate ANN surrogate models were also constructed for greater accuracy within these mouse groups. Thus, four distinct ANN surrogates are considered: 70 kDa nanocarrier control case, 70 kDa nanocarrier 3 mg/kg and 30 mg/kg DEX treatment cases, 500 kDa nanocarrier control case, and 500 kDa nanocarrier 3mg/kg and 30 mg/kg DEX treatment cases. For each case, the tumor transport model was parameterized by L_p and K. The discretized fluid and solute transport models were solved using the method of lines via the stiff QNDF solver in DifferentialEquations.jl[41] for data acquisition. Then, the spatially-averaged concentrations over a discrete time horizon of 5 minutes were taken as outputs.

A Sobol sequence sampling protocol[42] in Surrogates.jl[43] was used to generate a data set of 10^6 points within the bounds described in Table S2 of the SI. The data was then scaled using min-max normalization and randomly divided into a training set (70%) and test set (30%). The ANN models were trained and constructed using Flux.jl[44,45]. Architectures of 2-4 hidden layers, 16-32 nodes per hidden layer, and several different activation functions (sigmoid[46], tanh[46], gelu[47], and swish[48]) were considered. Through tuning and comparison, a two-hidden-layer model with 24 neurons each with the swish activation function was chosen for use in this work. This ANN model is depicted in Figure 3.

Due to the relatively small size of the ANNs, the models were trained using a combination of batch and mini-batch gradient descent with a mini-batch size of 10% of the training data set. The Adam optimizer was used for training with the standard mean-squared-error (MSE) loss function. The model was trained for 50 epochs using an early stopping criteria, with a MSE tolerance of 10^{-7}. The learning rate was kept constant at 10^{-3}. Following training, the MSE and mean relative percent error were evaluated on the test set. This training protocol was found to be effective, as indicated by the time and performance metrics listed in Table S3 of the SI.

In previous studies, recurrent neural network model architectures are utilized as a typical method to simulate dynamical systems by directly approximating the numerical integration function as opposed to the entire numerical integration procedure[49]. This method was not employed in this study as it would necessitate an iterative loop in the objective function (due to the feedback of information of earlier-time states) to create the concentration profile for each function evaluation. Such a process would introduce additional complexity that would negatively impact the solution times when included in deterministic global optimization routines used in this work.

2.4 | Simplified Parameter Estimation Problem

In this section, a simplified parameter estimation problem is proposed using ANN surrogate models introduced in Section 2.3. Similar to (1), we seek to minimize the SSE between the average concentration predicted by the ANN
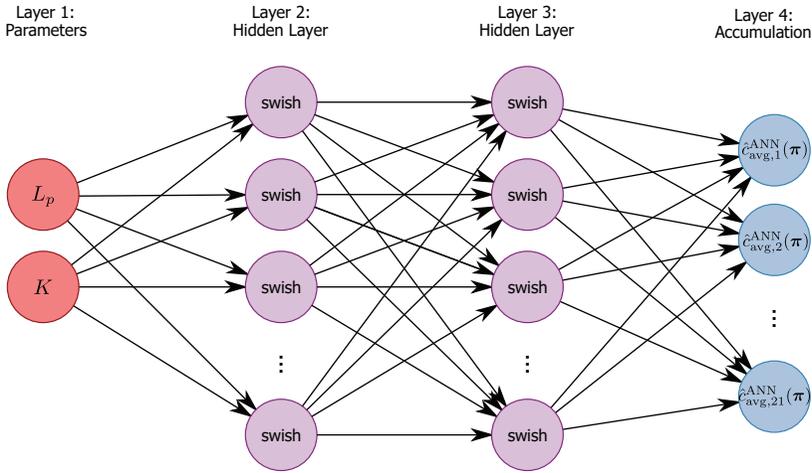
FIGURE 3 A fully connected feed-forward multilayer perceptron artificial neural network surrogate model is illustrated and represents the model architecture used for the simplified parameter estimation problems considered in this. The two node input layer (Layer 1) takes as input the physiological parameters L_p and K. These inputs feed to the two hidden layers using 24 nodes and the swish activation function. The outputs of the second hidden layer (Layer 3) are then passed to the output layer (Layer 4) consisting of 21 nodes, representing the temporally discretized accumulation profile.

surrogate model and experimental data over the entire time horizon, with inequality constraints on superficial IFP:

$$\min_{\boldsymbol{\pi} \in \Pi} \sum_{i=1}^{n} \left(\hat{c}_{\text{avg},i}^{\text{ANN}}(\boldsymbol{\pi}) - \hat{c}_{\text{avg}}^{\text{data}}(t_i) \right)^2 \tag{3}$$

$$\text{s.t. } \hat{p}_{peri}(\boldsymbol{\pi}) \leq \hat{p}_{peri,\text{max}}$$

$$\hat{p}_{peri}(\boldsymbol{\pi}) \geq \hat{p}_{peri,\text{min}},$$

where $\hat{c}_{\text{avg},i}^{\text{ANN}}$ represents the dimensionless spatial average nanocarrier concentration at discrete time node i calculated from the ANN model. The inequality constraints on the superficial IFP may be simplified and reformulated as equivalent inequalities that are linear in the optimization variables (model parameters) L_p and K utilizing the closed-form analytical solution for the IFP profile from Baxter and Jain [16]. This simplifies the problem significantly and, in turn, reduces the computational complexity of solving (3). The details of how this is done can be found in Section S3 of the SI.

The optimization formulation (3) can then be reformulated as:

$$\min_{\boldsymbol{\pi} \in \Pi} \sum_{i=1}^{n} \left(\hat{c}_{\text{avg},i}^{\text{ANN}}(\boldsymbol{\pi}) - \hat{c}_{\text{avg}}^{\text{data}}(t_i) \right)^2 \tag{4}$$

$$\text{s.t. } \pi_2 \leq \zeta_{\text{max}} \pi_1$$

$$\pi_2 \geq \zeta_{\text{min}} \pi_1,$$

where ζ_{max} and ζ_{min} are listed in Table 3 and are calculated based on the physical bounds on the superficial IFP listed in Table 1. The calculation procedure is described in the SI.

TABLE 3 The coefficients for the constraints on the superficial (peripheral) IFP are calculated for the control, 3 mg/kg, and 30 mg/kg DEX treatment cases in formulation (3) based on the IFP bounds previously reported. These values are used to ensure physically meaningful solutions are identified.

Dose	Control	3 mg/kg	30 mg/kg
ζ_{min} (cm)	0.2855	0.7355	1.5898
ζ_{max} (cm)	0.3967	1.0577	2.4447

2.5 | TME-Normalizing Therapy Design for Dose Selection

In this section, we propose a method for optimal TME-normalizing therapy design for dose selection with the overall objective of improving transport and accumulation of anticancer drugs within the tumor interstitium. To do so, we investigate the experimental effects of different doses of pretreatment DEX and utilize empirical correlations for optimal decision-making. Empirical correlations are required to construct a mathematical relationship between DEX dose and two important physiological parameters: vascular hydraulic conductivity L_p and interstitial hydraulic conductivity K. The purpose of this study is to propose a systematical mathematical methodology for TME-normalizing therapy design.

Based on the preclinical data obtained from Martin et al. [10], we utilize nonlinear regression with a rational model to establish the following relationships:

$$f_{L_p}^r(x) = \frac{-7.519 \times 10^{-8} x^2 + 3.355 \times 10^{-6} x + 6.944 \times 10^{-7}}{x + 0.6175}, \tag{5}$$

$$f_K^r(x) = \frac{-2.458 \times 10^{-8} x^2 + 2.524 \times 10^{-6} x + 2.916 \times 10^{-7}}{x + 0.7816}, \tag{6}$$

where x denotes pretreatment DEX dose (mg/kg), and the functions $f_{L_p}^r$ and f_K^r represent the values of L_p and K, respectively, following treatment with DEX, as predicted by the rational regression model.

Since the data obtained from Martin et al. [10] are limited to the three pretreatment DEX doses, we also wish to explore different dose-dependent relationships that could exist with other data sets. The purpose of this is to demonstrate the applicability of our proposed method with fictitious experimental data exhibiting complicated dose-dependent treatment relationships for pretreatment DEX doses between the actual data of 3 mg/kg and 30 mg/kg with dosages set at 10 mg/kg, 15 mg/kg, 20 mg/kg, and 25 mg/kg.

The original data, fictitious data, and corresponding polynomial regression models are plotted in Figure 4. The regression equations are given by:

$$f_{L_p}^p(x) = -6.23 \times 10^{-13} x^5 - 5.96 \times 10^{-11} x^4 + 5.61 \times 10^{-9} x^3 - 1.272 \times 10^{-7} x^2 + 8.797 \times 10^{-7} x + 1.131 \times 10^{-6}, \tag{7}$$

$$f_K^p(x) = 1.139 \times 10^{-11} x^5 - 8.389 \times 10^{-10} x^4 + 2.183 \times 10^{-8} x^3 - 2.421 \times 10^{-7} x^2 + 1.093 \times 10^{-6} x + 3.798 \times 10^{-7}, \tag{8}$$

where x is the DEX dose as before, and $f_{L_p}^p$ and f_K^p represent the values of L_p and K, respectively, following treatment with DEX, as predicted by the polynomial regression model.

The TME-normalizing therapy design problem is formulated as the following NLP:

$$\max_{x \in X} \hat{c}_{avg}\left(t_f, \left(f_{L_p}^j(x), f_K^j(x)\right), d_m\right), \tag{9}$$
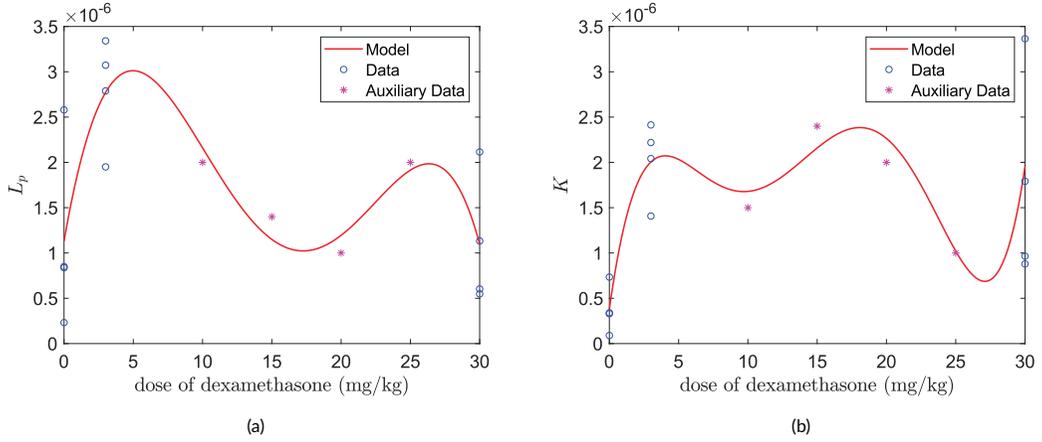
FIGURE 4 Experimental data and corresponding regression models for (7) and (8) are respectively plotted in (a) L_p versus dose; (b) K versus dose of dexamethasone. Auxiliary, fictitious data are considered to demonstrate the applicability of the proposed approach to complex dose-dependent relationships that could exist naturally.

with $j \in \{r, p\}$. The objective is to seek an optimal dose that maximizes the spatial average nanocarrier concentration $\hat{c}_{\text{avg}}$ in the tumor interstitium at $t_f = 5$ min. The function $\hat{c}_{\text{avg}}$ is evaluated by the numerical solution of the solute transport model, and the correlations between hydraulic conductivities and DEX doses are established as (5) and (6) for the existing data, and (7) and (8) for the fictitious data.

2.6 | Drug Size Design

In this section, the practicability of the tumor transport model for drug size design problems is addressed. After the optimal dose of pretreatment DEX is determined and a patient's response to that treatment is quantified, an anticancer nanocarrier is designed that results in optimal delivery to the tumor interstitium. For example, a nanoparticle size can be *tuned* for a patient-specific tumor pathophysiology.

After DEX pretreatment, it is desirable to determine an optimal nanocarrier size that can maximize the drug concentration in the interstitial space of the tumor. Alteration in pharmacokinetics, such as distribution and excretion, can have a substantial influence on achieving the desired therapeutic concentration of a particular nanocarrier. A very high concentration may result in side effects or toxicity. A very low concentration will be ineffective. In this situation, an optimal therapy requires a strict guarantee of some safety/performance specifications. The drug size design problem is formulated as a PDE-constrained NLP to account for these potential requirements:

$$\max_{d_m \in Z} \hat{c}_{\text{avg}}(t_f, \boldsymbol{\pi}, d_m) \tag{10}$$

$$\text{s.t.} \quad \hat{c}_{peri}(t_f, \boldsymbol{\pi}, d_m) \leq \lambda_1$$

$$\hat{c}_{peri}(t_f, \boldsymbol{\pi}, d_m) \geq \lambda_2,$$

where t_f is the final time ($t_f = 5$ min), $\hat{c}_{peri}$ is the dimensionless nanocarrier concentration in the superficial area of

tumor (g/mL). The mappings between physiological parameters that are directly related to the nanocarrier sizes are established and introduced in Section S4 of the SI. For this work, we use $\lambda_1 = 4.5$ as the threshold for the safety constraint, which is double the periphery nanocarrier concentration for the 3 mg/kg DEX treatment case. Further, we use $\lambda_2 = 3.6$ as the performance constraint, which is chosen based on periphery nanocarrier concentration for the control case. Note that these thresholds are merely chosen for demonstrating the drug size design approach and how to deal with the situation that a design is implemented under potential performance/safety requirements.

Furthermore, we propose a therapy design strategy that simultaneously seeks an optimal dose of DEX and an optimal nanocarrier size that maximizes the nanocarrier concentration accumulation inside the tumor interstitial space:

$$\max_{x \in X, d_m \in Z} \hat{c}_{\text{avg}} \left(t_f, \left(f_{L_p}^j(x), f_K^j(x) \right), d_m \right) \tag{11}$$
$$\text{s.t.} \quad \hat{c}_{peri} \left(t_f, \left(f_{L_p}^j(x), f_K^j(x) \right), d_m \right) \leq \lambda_1$$
$$\hat{c}_{peri} \left(t_f, \left(f_{L_p}^j(x), f_K^j(x) \right), d_m \right) \geq \lambda_2,$$

with $j \in \{r, p\}$. This formulation provides an alternative methodology for neoadjuvant therapy that could identify a possible therapy and nanocarrier size combination that leads to improved transport and accumulation over the individual results determined by the sequential design approach.

ANN surrogate models are also proposed for the simultaneous design problem (11) to reduce the computational burden over the PDE-constrained problem. To accomplish this, two ANNs are established each with L_p, K, and d_m as inputs. The respective ANNs each have a single output $\hat{c}_{avg}^{\text{ANN}}$ and $\hat{c}_{peri}^{\text{ANN}}$. Note that these ANN models are different from the one introduced in Section 2.3. To train these new ANNs, a Sobol[42] sequence sampling method was used again to create a 10^6 point data set on the domain $(Lp, K, d_m) \in [5 \times 10^{-7}, 5 \times 10^{-6}] \times [5 \times 10^{-7}, 5 \times 10^{-6}] \times [10, 60]$. Consistent with the parameter estimation of the ANN models, the data set was scaled using a min-max normalization and divided randomly into training (70%) and validation (30%) sets. Training was performed using Flux.jl with the Adam optimizer with a learning rate of 10^{-4}. Each ANN model for $\hat{c}_{avg}^{\text{ANN}}$ and $\hat{c}_{peri}^{\text{ANN}}$ has two hidden layers with 12 neurons using the tanh activation function. The models were trained using an equivalent protocol to that described in Section 2.3. The benchmarks for data generation, training time, and performance are shown in Table S5 of the SI.

The formulation with ANN models for the simultaneous design approach can be expressed as:

$$\max_{x \in X, d_m \in Z} \hat{c}_{\text{avg}}^{\text{ANN}} \left(\left(f_{L_p}^j(x), f_K^j(x) \right), d_m \right) \tag{12}$$
$$\text{s.t.} \quad \hat{c}_{peri}^{\text{ANN}} \left(\left(f_{L_p}^j(x), f_K^j(x) \right), d_m \right) \leq \lambda_1$$
$$\hat{c}_{peri}^{\text{ANN}} \left(\left(f_{L_p}^j(x), f_K^j(x) \right), d_m \right) \geq \lambda_2.$$

2.7 | Settings for Solving Optimization Problems

The settings used in this study for the numerical methods and software packages are discussed in this section. For the parameter estimation, TME-normalizing therapy design, and drug size design problems, the spatial domain for both fluid transport and solute transport models are discretized into $N = 100$ nodes. The simulation time horizon contains 21 time nodes (5 min). Based on the superficial region (around 0.07 mm from surface)[50] and the average tumor diameter (0.6 - 1.1 cm) in the DEX treatment research[10], we choose $n = 99$ to account for the superficial region of the tumor. The physiological parameters used in the tumor transport model are provided in Table S6 of the SI. The parameter estimation, drug size design, and TME-normalizing therapy design problems are all solved to

global optimality using the EAGO [31] v0.6.1 solver via JuMP v0.21.4 [51] in the Julia programming language [40]. Custom bounding routines with the mixed IA/AA method and standard DI are utilized in the B&B algorithm for solving the parameter estimation and drug size design problems. For the parameter estimation problems, the absolute global convergence tolerance is set as 10^{-6}, and the relative global convergence tolerance is set as 10^{-1} for each case. For the drug size design and TME-normalizing therapy design problems, the absolute convergence tolerance is set as 10^{-6}, and the relative convergence tolerance set as 10^{-2}. Each problem was run on a personal workstation with an Intel Xeon E3-1270v5 4-core/8-thread CPU operating at 3.60GHz/4.00GHz (base/turbo) frequency and 32GB ECC RAM running Windows 10 Version 2004.

3 | RESULTS AND DISCUSSION

3.1 | Global Optimization Results for Model Validation

In this section, the global optimization results are discussed for the parameter estimation problems. The global optimal solutions obtained from the parameter estimation problems for different doses of DEX treatment cases are listed in Table 4 for each formulation with the original mechanistic tumor transport model (1) as well as the ANN surrogate model (4). Note that the dose selection for the experiments was based on previous work, which confirmed 3 mg/kg DEX as the lowest dose to reduce IFP. Additionally, this dose is similar to that used in the clinical trials of CDDP/m (NCT02043288) [52]. The global solutions found for both the mechanistic model and ANN model are very close to one another, with the relative error for each case being within 2.5%. This certifies the accuracy of the ANN surrogate models and the validity of the inequality constraints simplifications. In Martin et al. [10], we obtained local optima for the parameter estimation problems. In that work, it was found that the estimated L_p value for 3 mg/kg DEX treatment case with 500 kDa nanocarrier injection exhibited a decreasing trend from the control case, whereas in this study we found an increasing trend. This does not represent a contradiction, as the parameter estimation problems differ significantly in that they consider different simulation time horizons. Furthermore, in the case of Martin et al. [10], no inequality constraints on the IFP were considered.

TABLE 4 Global optima for parameter estimation problems using the mechanistic model (1) and the ANN model (4). It is noted that the solutions obtained for the ANN surrogate model are very close to those obtained for the mechanistic model. This is to be expected since a high-degree of accuracy of the ANN was obtained when training. The unit for L_p^* is cm/mm Hg-sec and for K^* is cm^2/mm Hg-sec.

Dextran molecular weight		70 kDa			500 kDa	
Dose	Control	3 mg/kg	30 mg/kg	Control	3 mg/kg	30 mg/kg
P_{eff} (cm/sec)	9.60×10^{-7}	4.61×10^{-6}	2.80×10^{-6}	8.18×10^{-7}	4.30×10^{-6}	1.62×10^{-6}
L_p^* - mechanistic model	8.51×10^{-7}	2.80×10^{-6}	1.12×10^{-6}	8.62×10^{-7}	2.22×10^{-6}	7.50×10^{-7}
L_p^* - ANN model	8.39×10^{-7}	2.77×10^{-6}	1.12×10^{-6}	8.43×10^{-7}	2.22×10^{-6}	7.50×10^{-7}
K^* - mechanistic model	3.35×10^{-7}	2.03×10^{-6}	1.80×10^{-6}	3.34×10^{-7}	2.34×10^{-6}	1.21×10^{-6}
K^* - ANN model	3.32×10^{-7}	2.04×10^{-6}	1.78×10^{-6}	3.29×10^{-7}	2.36×10^{-6}	1.20×10^{-6}

The time costs for each model are reported in Table 5. For DEX treatment cases, the parameter estimation problems with the mechanistic model and the proposed customized bounding routines are extremely computationally expensive. Despite using the most efficient global bounding method considered, these problems still required hours

or even days to solve. In contrast, the parameter estimation problems for DEX treatment cases using the ANN surrogate models can be solved within one minute. Even accounting for the time costs of generating data and training, the ANN surrogate models significantly reduce the burden of solving the parameter estimation problems to global optimality. Interestingly, it takes about an order-of-magnitude longer to solve the parameter estimation problems for the control cases with ANN models versus the mechanistic models. In these cases, it is observed that the lower-bounding problems solved for the ANN problems furnish weaker bounds than for the mechanistic modeling case, resulting in slower convergence of the B&B algorithm.

TABLE 5 The computational time costs for the parameter estimation problems using the mechanistic model (1) and the ANN model (4). Barring the control case, solving the PDE-constrained optimization problem (1) requires significantly more time than the the problem with the ANN (4), which does not account for the ANN training time.

Dextran molecular weight	70 kDa			500 kDa		
Dose	Control	3 mg/kg	30 mg/kg	Control	3 mg/kg	30 mg/kg
Mechanistic model (s)	8.5	169558.3	238732.2	8.1	398792.2	50368.1
ANN model (s)	97.9	7.3	25.8	23.2	17.6	18.8

3.1.1 | Interstitial Fluid Pressure and Velocity Profiles

Previous studies showed that an important barrier to drug delivery in the TME is the elevated IFP resulting in reduced pressure gradients across the vessel wall[15]. This is due to the interstitial hypertension phenomenon[9] caused by leaky blood vessels and the lack of functional lymphatic vessels, which drain excess fluid from tumor tissue. TME-normalizing therapy can repair the abnormal vasculature and reduce IFP, resulting in a higher pressure gradient for higher transvascular and interstitial fluid flow. Thus, we quantified the IFP with different doses of DEX treatment to characterize the TME normalization process. The dimensionless IFP profiles as functions of dimensionless radial position with respect the optimal solutions (i.e., from Table 4) are illustrated in Figure 5(a). The IFP profiles tend to reach a steady-state pressure p_{ss} at the center of the tumor, where the IFP equals the vascular pressure p_v. However, in the periphery, the IFP rapidly decreases with increasing distance from the tumor center. This finding is consistent with previous mathematical models[16] and experimental findings[15]. Thus, the IFP profiles indicate that the extravasation of fluid from blood vessels is extremely slow near the center, whereas it is highest at the periphery due to lower IFP leading to an increased transvascular pressure gradient. In addition, the model confirms that DEX reduces the spatially-averaged IFP and therefore establishes a more advantageous transvascular pressure gradient that contributes to enhanced transvascular fluid flow[10], that will further affect the interstitial fluid transport.

The interstitial fluid velocity (IFV) is generated from the interior IFP gradient by Darcy's law (introduced in Section S1.1 of the SI). To investigate the effects of TME normalization on interstitial fluid transport, we quantified the normalized IFV ($\hat{u} = uR/(K(p_{ss} - p_\infty))$) profiles for different doses of DEX. A positive value of IFV indicates that the interstitial fluid flow is from the center to the periphery of the tumor. As illustrated in Figure 5(b), we observed that the normalized IFV is very low around the center and increases towards the periphery where there is the highest flow rate. The dimensionless parameter $\alpha = R\sqrt{L_p S/KV}$ (introduced in S1.1 of the SI), which is a measure of the ratio of interstitial to vascular resistances of fluid flow, represents the gradient of increase of normalized IFV. Summarily, a larger value for α indicates a steeper increase in the normalized IFV profile with increasing distance from tumor center. The model-predicted α values for the control, 3 mg/kg DEX treatment, and 30 mg/kg DEX treatment cases from the
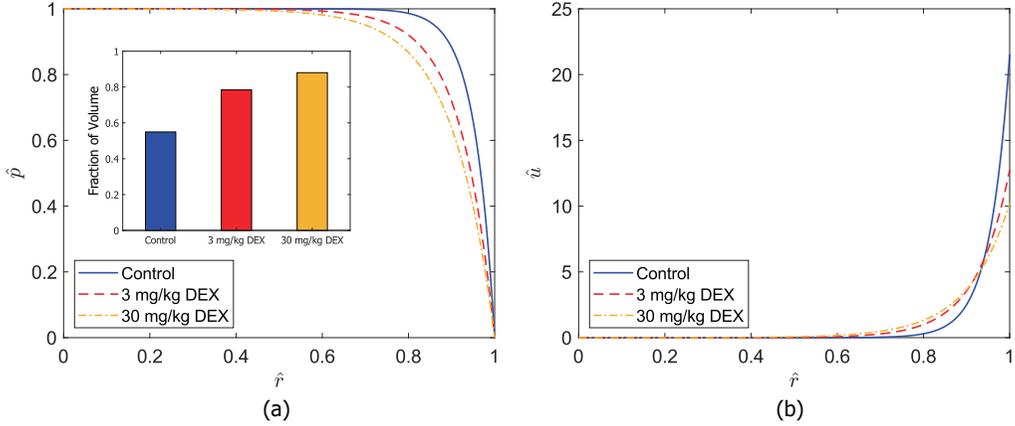
FIGURE 5 Radial dose-dependent interstitial fluid pressure and velocity profiles. (a) Mathematical model-generated profiles of dimensionless interstitial fluid pressure (IFP) $\hat{p} = (p - p_\infty)/(p_{ss} - p_\infty)$ versus the dimensionless tumor radial position $\hat{r}$ from vessel permeability data collected using fluorescently-labelled 500 kDa dextran in control tumors and tumors in mice treated with 3 mg/kg and 30 mg/kg dexamethasone (DEX) daily for four days are presented. Spatially-averaged IFP is reduced with DEX treatment. The interior bar graph illustrates the fraction of tumor volume that has a favorable transvascular pressure gradient (i.e. $\hat{p} \leq 0.9933$). This IFP threshold is determined by the region with $\hat{r} \geq 0.6$ for the 3 mg/kg DEX treatment case, which is taken as the volume with favorable transvascular pressure gradient. (b) Normalized interstitial fluid velocities (IFV) $\hat{u} = uR/(K(p_{ss} - p_\infty))$ are plotted versus dimensionless tumor radial position $\hat{r}$. Greater IFVs are achieved deeper in the tumor interstitium following DEX treatment with a reduction in velocity nearest the tumor periphery. This results in increased interstitial transport of nanocarriers.

500 kDa dextran experimental data are 22.521, 13.756 and 11.219, respectively. Thus, compared to the control, the treated cases have smaller values of α that indicate a gradual increase in normalized IFV from the center tumor over a larger fraction of tumor volume. Note that the normalized IFV neglects the influence of interstitial hydraulic conductivity K. However, K is larger by an order of magnitude for DEX treated cases than the control case (Table 4). Thus, the actual IFV for DEX treated cases is always higher than the control case. Although, we reported in Martin et al. [10] that DEX treatment increases the perfused vascular density, we assumed in the current study that the tumor radius R and vascular density S/V do not vary significantly between each case. Thus, a reduction in the ratio of the vascular hydraulic conductivity to the interstitial hydraulic conductivity (i.e., L_p/K) is the major reason for a reduction in α. A smaller value of L_p/K indicates a larger proportion of interstitial fluid transport. Therefore, a less steep normalized IFV profile resulting from a smaller α caused by a reduction of L_p/K implies enhanced interstitial fluid transport by vascular and ECM normalization.

3.1.2 | Solute Concentration Profiles

We next sought to determine the drug distribution within tumors by obtaining solute concentration profiles from the IFP and IFV profiles. The IFP gradient induces transvascular convective transport, the IFV profiles reflect interstitial convective transport, and the solute concentration gradient induces interstitial diffusive transport. Figure 6 illustrates the model-predicted solute concentration profiles with respect to dimensionless tumor radial position $\hat{r}$ for the 500

kDa dextran experimental data, with the vascular concentration following an exponential decay post-administration.
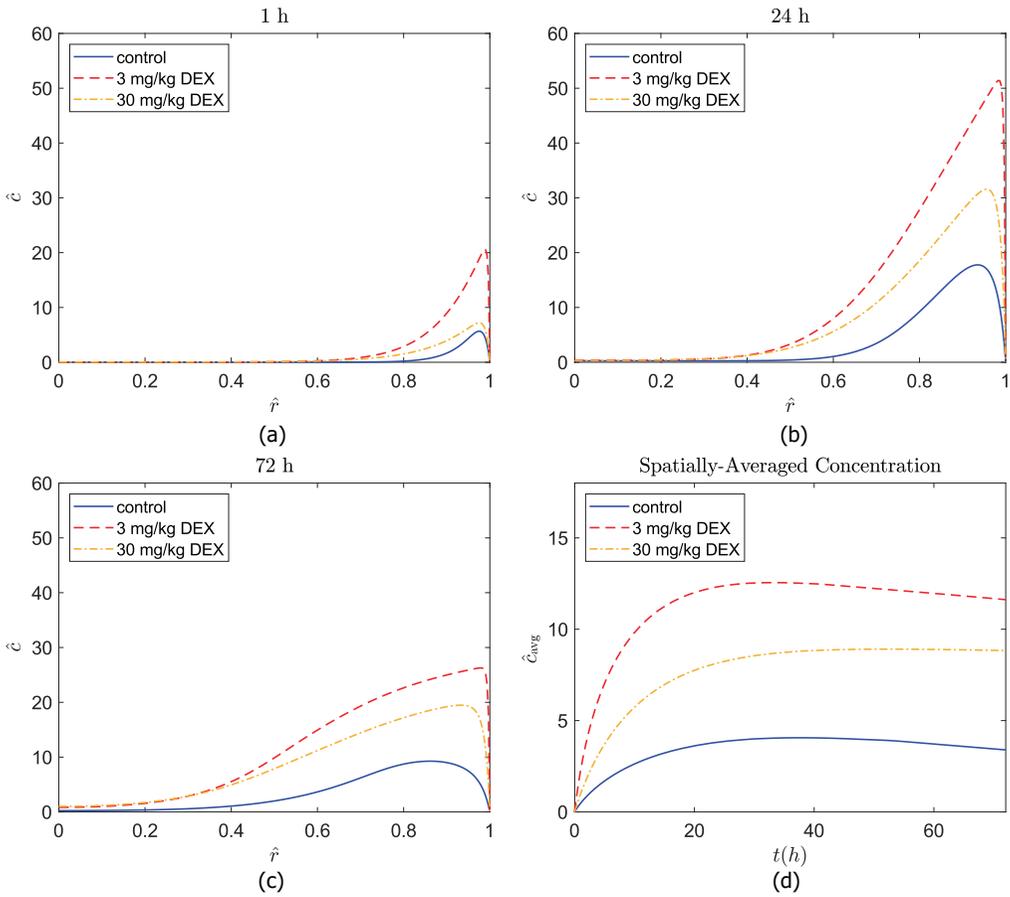

FIGURE 6 Radial and temporal dose-dependent solute concentration profiles. Interstitial concentrations $\hat{c}$ of 500 kDa dextran are plotted versus dimensionless tumor radial position $\hat{r}$ for a vascular concentration with a half-life of around 21 h for the control, 3 mg/kg DEX treatment, and 30 mg/kg DEX treatment cases at (a) 1 h; (b) 24 h; (c) 72 h post-administration. (d) Spatially-averaged interstitial concentrations $\hat{c}_{avg}$ are plotted versus time. After DEX treatment, the overall solute concentration accumulation is increased inside the tumor. The 3 mg/kg DEX treatment case results in the highest overall concentration accumulation.

As illustrated in Figure 6(a), the interstitial concentration at 1 h post-administration of the dextran is equal to the normal tissue concentration (equals 0 in dimensionless form) at the periphery and quickly increases to a peak in the peripheral region where there is a higher transvascular pressure gradient, which significantly enhances transcapillary convective solute transfer. The fraction of tumor volume that has a higher transvascular pressure gradient is graphed for each treatment group in the inset of Figure 5(a). Simultaneously, the higher IFV in the peripheral region causes a higher interstitial fluid flux that carries the solute outwards to the periphery. As a result, the solutes accumulate and reach peak concentration near the periphery, then decrease to zero at around $\hat{r} = 0.8$ for the control case and $\hat{r} = 0.6$ for the 3 mg/kg and 30 mg/kg DEX treatment cases. Indeed, the region with favorable transvascular pressure

gradient for DEX treated cases is larger than the control case (Figure 5(a)). This pressure gradient leads to a enhanced convective transvascular transport that carries solutes into the interstitial space of a larger proportion of the tumor. In other words, the region with higher solute accumulation occurs over a longer fraction of tumor radius for the DEX treatment cases compared to control.

As presented in Figure 6(b), the interstitial concentration profiles for all treatment cases have higher peaks at 24 h than 1 h. The concentration peaks for all cases at 72 h (Figure 6(c)) are lower than 24 h but higher than 1 h. This is because the vascular concentration decays at 72 h compared with 24 h so that there are fewer nanocarriers to be carried by transvascular flow into the interstitial space. In addition, we found that the interstitial concentration profiles at 72 h become flatter than 24 h with a higher concentration retained towards the middle of the tumors, such as at $\hat{r} = 0.5$. This is caused by the slower interstitial diffusion generated from the concentration gradient that gradually transfers nanocarriers from the concentration peak in the periphery towards the tumor center, where the concentration of nanocarriers is near zero. The transvascular flow is limited at 72 h due to the systemic clearance of circulating nanocarriers, but the diffusion caused by concentration gradient becomes more evident in the flatter concentration profiles.

As illustrated in Figure 6(d), the spatially-averaged interstitial concentration rises to a peak and stays steady after that. Although the vascular concentration of nanocarriers decays exponentially, the spatially-averaged interstitial concentrations decrease slowly after reaching the peak. The concentration profiles at the time with respect to the highest spatially-averaged concentration accumulation are illustrated in Figure S2 of the SI. We observed that the highest spatially-averaged concentration occurs at 38.8 h, 34.2 h and 53.9 h for the control, 3 mg/kg and 30 mg/kg DEX treatment cases, respectively. In general, the nanocarriers accumulate to a peak concentration in the first dozens of hours and then decrease with a slow rate.

The spatially-averaged concentrations at 72 h are 84%, 92% and 99% of their highest concentrations for the control, 3 mg/kg and 30 mg/kg DEX treatment cases, respectively (illustrated in Figure S3 of the SI). We found that the spatially-averaged concentrations of the 500 kDa dextran in control tumors only decrease by 16% in 33.2 h after reaching highest concentration, indicating a retention effect. The 3 mg/kg and 30 mg/kg DEX treatments both enhance this retention effect (92% and 99% are higher than the control case). Though the 3 mg/kg DEX treatment does not result in the highest percentage of retention at 72 h (92% < 99%), it has the highest spatially-averaged concentration throughout the whole time horizon. In contrast, the control case has the lowest percentage and also the lowest spatially-averaged concentration. Thus, these findings demonstrate that DEX treatment not only increases permeability [10] but also retention towards promoting the EPR effect.

We further investigated the relation between the solute concentration distribution over time and dose of DEX treatment. The concentration profile for the 30 mg/kg DEX treatment case is closer to the control case at 1 h post-administration, whereas it is closer to the 3 mg/kg DEX treatment case at 72 h post-administration. At 1 h post-administration, there are many nanocarriers in perfused vessels and they are carried into the tumor tissue by transvascular flow. A larger vascular hydraulic conductivity L_p indicates higher transvascular flow rate. However, L_p for 30 mg/kg DEX treatment case is closer to the control case (Table 4). Although the vessels are normalized after 30 mg/kg DEX treatment, there is too much pericyte coverage that reduces the vessel wall pore size [10] thereby limiting nanocarrier extravasation at 1 h post-administration. In contrast, the extravasation of nanocarriers is trivial at 72 h due to the decay of its concentration in the vasculature and the interstitial concentration profile has already reached a peak and decreased. Thus, the interstitial diffusive transport becomes more prominent. Since both 3 mg/kg and 30 mg/kg DEX treatment similarly reduce hyaluronan levels and tissue stiffness [10], resulting in much larger interstitial hydraulic conductivity K than the control case (Table 4), the enhanced interstitial diffusive transport results in the observed profiles. In addition, we found that the 3 mg/kg DEX treatment case results in a much higher overall nanocarrier concentration

accumulation in the tumor tissue than that of the control and the 30 mg/kg cases at all time nodes (1 h, 24 h, and 72 h), indicating increased delivery of anticancer nanocarriers leading to improved efficacy as demonstrated in Martin et al. [10]. Given that the 3 mg/kg DEX treatment lead to the highest nanocarrier accumulation, we next investigated the convective and diffusive transvascular fluxes separately to understand how DEX increased accumulation.

3.2 | Dexamethasone Increases Convective Transvascular Flux in Tumors

After finding the interstitial concentration profiles that dictate enhanced nanocarrier distribution and accumulation with DEX treatment, we hypothesized that the difference in concentrations between the control and DEX treatment cases depends on the relative contributions of convective and diffusive transvascular flux. Previous studies indicated that the main mechanism of transvascular transport is diffusion because elevated IFP in the TME abrogated the transvascular pressure gradient [1]. We reasoned that, because DEX reduces IFP, it could enhance convective flux, which leads to more rapid transport than diffusive flux. However, the relative contributions from convection and diffusion throughout the entire volume of a tumor have never been studied before.

Based on the optimal hydraulic conductivity values determined by global optimization, we first quantified the model-predicted transvascular convective and diffusive fluxes. As described in (2), the convective flux is calculated by $L_p \frac{S}{V}(p_v - p)(1 - \sigma)c_v$ and the diffusive flux is calculated by $P\frac{S}{V}(c_v - c)\frac{Pe}{e^{Pe}-1}$. The relative contributions from convective and diffusive flux to the spatially-averaged concentration profile with time are illustrated in Figure S4. We found that the convective flux contribution for the DEX treatment case is dominant throughout the time horizon compared with the control case. This indicates that the normalized TME after DEX treatment is advantageous for convective transport.

To better understand the effects of TME normalization on transvascular transport, we sought to determine the spatial dependence of model-predicted diffusive and convective fluxes in tumors. In Martin et al. [10], we performed continuous intravital microscopy on mice for one hour post-administration and investigated nanocarrier microdistribution. Here, we quantified the spatial convective and diffusive fluxes at one hour post-administration to study their distribution in tumors. As shown in Figure 7(a), in the region with $\hat{r} < 0.8$, the convective flux is near zero while diffusion is the main mode of transport. This is because the IFP is close to the microvascular pressure (Figure 5 (a)), indicating that there is no driving force for convection. Diffusion, although dominant, is small, and so there is not much transvascular flux in the tumor center. In contrast, in the region with $\hat{r} > 0.8$, there is more convective than diffusive flux, with the latter being near zero. This convective flux at the periphery is 22-fold greater than the diffusive flux at the center. The reason for this is that the IFP in the convection-dominated region is low (Figure 5 (a)), which induces a high transvascular convective flux driven by a large pressure gradient. Accordingly, the convective transport increases the interstitial concentration, thereby lessening the concentration gradient and reducing the driving force for diffusion. In addition, the Pe number, which represents the ratio between transvascular convection and diffusion rates, is very large in the periphery, reflecting the extremely small diffusive flux as observed in Figure 7(a). As a result, we found that there is a convection-dominated region and a diffusion-dominated region and the maximum rate of convective flux is an order-of-magnitude greater than the maximum diffusive flux.
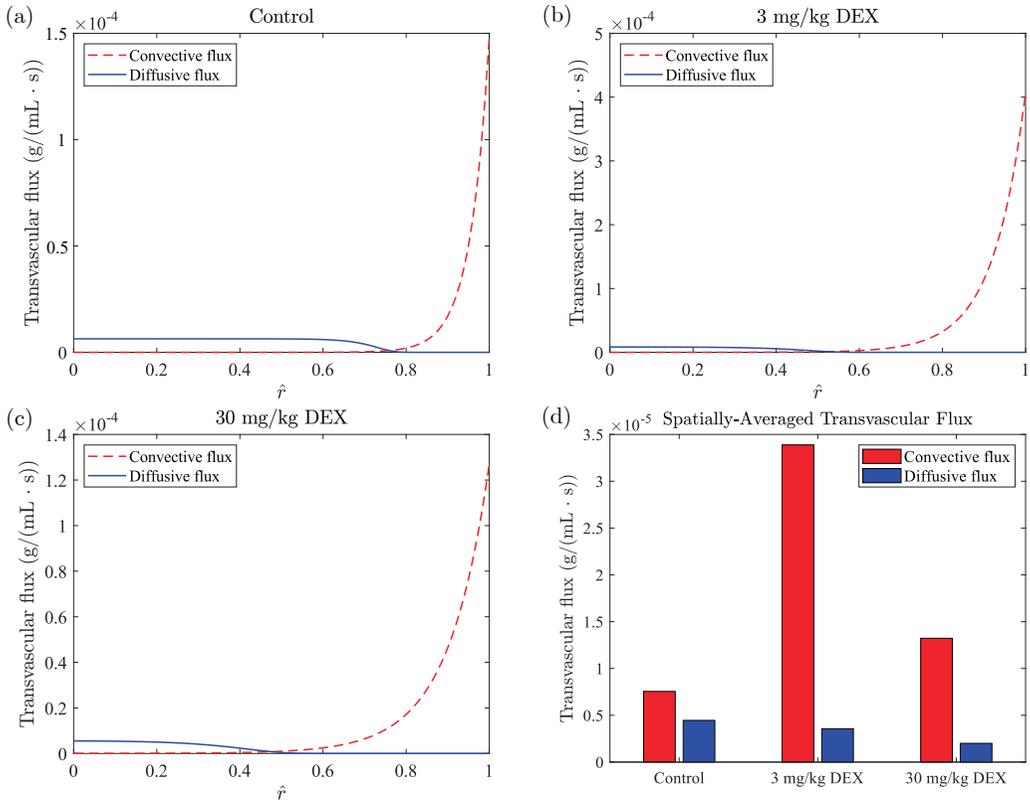
FIGURE 7 Dose-dependant transvascular convective and diffusive flux profiles. The transvascular flux profiles of 500 kDa dextran over the dimensionless tumor radial position $\hat{r}$ one-hour post-administration are plotted for the (a) control; (b) 3 mg/kg dexamethasone (DEX) treatment; and (c) 30 mg/kg DEX treatment cases. (d) The spatially-averaged convective and diffusive fluxes at one-hour post-administration for different doses of DEX are presented in this bar plot. General trends show greatest convective flux at the tumor periphery and greatest diffusive flux deeper at the tumor center. Following DEX treatment, convection accounts for a greater proportion of the spatially-averaged transvascular fluxes, demonstrating how TME normalization induces a larger transvascular pressure gradient that is advantageous for improving nanocarrier delivery in tumors. The 3 mg/kg DEX treatment induces highest convective flux, indicating that a moderate dose of DEX is more advantageous for enhancing convective transport.

Next, we investigated the effect of TME normalization on the spatial distribution of these fluxes. As illustrated in Figure 7(b), the maximum convective flux at the periphery for 3 mg/kg DEX is 48-fold greater than the maximum diffusive flux, which occurs in the tumor center. Since the maximum diffusive flux is close to the control case, this indicates that convection is greatly enhanced and responsible for a larger proportion of total transvascular transport in the normalized TME after treatment with 3 mg/kg DEX. In contrast, in Figure 7(c), the maximum convective flux for 30 mg/kg DEX is 22-fold greater than the maximum diffusive flux, which is comparable to that of the control case. In fact, by comparing the values of maximum convective flux at the periphery, we found that the flux for 30 mg/kg DEX is 14.3% less than the control case. The reason is that the vascular hydraulic conductivity L_p for with 30 mg/kg DEX treatment is 13% less than the control case (Table 4). This is because DEX normalizes the vessels, increases vessel

maturity, and thereby reduces vessel leakiness. As a result, the vascular hydraulic conductivity reduces, leading to the lower maximum convective flux at the tumor periphery. However, these findings do not indicate that the convective flux for 30 mg/kg DEX reduces throughout the entire tumor compared to the control. This is because we also found that the volume of the convection-dominated region is much larger for DEX treatment cases.

As illustrated in Figure 7(b) and Figure 7(c), the convective flux for both 3 and 30 mg/kg DEX treatment cases begins to increase around $\hat{r} = 0.6$ versus $\hat{r} = 0.8$ for the control case, indicating a larger convection-dominated region. These findings are illustrated in Figure 8, which shows a schematic of tumor cross sections for the control case and 3 mg/kg DEX treatment case. Note that the 30 mg/kg DEX treatment case has almost the same proportion of convection-to-diffusion-dominated region as the 3 mg/kg case. Thus, the 3 mg/kg DEX was chosen to illustrate the treatment case in Figure 8. We found that the tumor volume fraction of convection-dominated region for the control case is only 49%, whereas this jumps to 78% for a tumor treated with DEX. This represents a 61% increase in the volume fraction of the tumor that is dominated by convective transport as a result of TME normalization with DEX treatment. Note that the transvascular fluxes in Figure 8 are scaled according to the 70 kDa dextran, and the corresponding convective and diffusive flux profiles are presented in Figure S5. The findings using the 70 kDa dextran to determine the convection- and diffusion-dominated regions are consistent with those using the 500 kDa dextran, as shown in Figure 7. Both doses almost equally increase the volume of the convection-dominated region, but the 3 mg/kg DEX is superior because it also significantly increases the maximum convective flux.

To quantify the contributions of convection and diffusion throughout the tumor, we assessed the spatially-averaged transvascular convective and diffusive fluxes and presented them in a bar plot as illustrated in Figure 7(d). We observed a 360% increase in convective flux with 3 mg/kg DEX and a 80% increase with 30 mg/kg DEX compared to the control case. This indicates that DEX dose has a significant impact on convective transport. It turns out that a moderate dose of DEX greatly enhances convection. Excess DEX still enhances convective transport, but much less effectively. The reason is that the vascular hydraulic conductivity L_p for 30 mg/kg DEX is much less than 3 mg/kg DEX (Table 4). In addition, we found that a higher dose of DEX treatment leads to a lower spatially-averaged diffusive flux (20% decrease with 3 mg/kg DEX and 65% decrease with 30 mg/kg DEX compared to control). One reason is that the elevated convective flux with DEX treatment results in a much higher interstitial concentration. Thus, the driving force from transvascular concentration gradient decreases, leading to a lower diffusive flux. In addition, we reported in Martin et al. [10] that the vessel wall pore size is smaller with 30 mg/kg DEX treatment because vascular normalization reduces vessel leakiness by shrinking vessel wall pores. Accordingly, the diffusive hindrance (introduced in S1.3 of the SI) is also smaller. Note that a smaller diffusive hindrance represents higher impairment to diffusion [7]. Thus, 30 mg/kg DEX treatment results in a lower diffusive flux. In conclusion, these results demonstrate that DEX increases the accumulation of nanocarriers in tumors by increasing the convective transvascular flux, but the dose of TME normalization treatment should be titrated to avoid reducing vessel wall pore sizes that limit the benefit to enhanced convection.
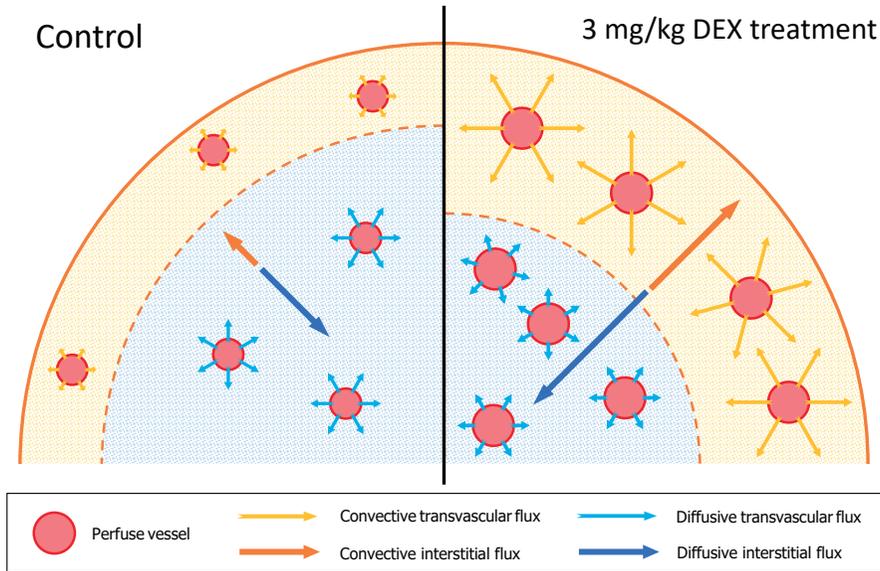
FIGURE 8 Cross sections of the spherical tumor are illustrated in this schematic for the control (left) and 3 mg/kg DEX treatment (right) cases. Perfuse vessels are more abundant and have a larger average diameter following DEX treatment versus the control case; a result of normalizing the tumor microenvironment. The outer orange shaded sections represent the convection-dominated region with significant pressure gradients resulting in predominant convective transvascular flux (yellow arrows). The inner blue shaded sections represent the diffusion-dominated region with almost no pressure gradient (highest interstitial fluid pressure (IFP)) resulting in predominant diffusive transvascular flux (light blue arrows). The blue region is much larger for the control case with the demarcation (orange dashed curves) between regions occurring at $\hat{r} = 0.8$, whereas the demarcation between regions for the DEX treatment case is at $\hat{r} = 0.6$. Convective transvascular flux is significantly enhanced after DEX treatment. The orange arrows pointing radially outward and blue arrows pointing radially inward represent, respectively, the nanocarrier convective and diffusive flux in the tumor interstitium. The direction of interstitial convective transport of nanocarriers is outward towards the periphery, caused by the IFP gradient, while the direction of interstitial diffusive transport of nanocarriers is inward towards the center, caused by the concentration gradient. The overall interstitial fluxes are significantly greater following DEX treatment. The interstitial fluxes and transvascular fluxes are illustrated based on the global optimization results for 13 nm nanocarrier experiments. Note that the interstitial and transvascular flux arrow lengths are each normalized to their own relevant bases for ease of illustration and should not be compared to one another. Also note that since interstitial fluxes are spatially dependent, the arrows represent spatially-averaged fluxes.

3.3 | Global Optimization Reveals Dose of Dexamethasone Maximizing Nanocarrier Accumulation

Given that a moderate dose of DEX is superior to no DEX and a high dose of DEX for enhancing transvascular transport, we hypothesized that there is an optimal dose of DEX that can maximize nanocarrier or antibody concentration accumulation. As indicated by the previous preclinical study [10], DEX as a drug for TME normalization is both (1) an antiangiogenic agent that can normalize tumor vessels and (2) a cancer-associated fibroblast reprogramming agent that reduces ECM levels leading to decompressed tumor vessels. The functions of (1) and (2) are associated with

vascular hydraulic conductivity L_p and interstitial hydraulic conductivity K, respectively. Both L_p and K become more favorable for drug delivery with a moderate dose of DEX treatment, but the relative contributions of (1) and (2) cannot be directly controlled with a drug like DEX that affects both. In addition, as indicated by Table 4, an excess dose of DEX decreases L_p thereby limiting transvascular flux for drug delivery. Thus, it is not clear what dose of DEX should be used to maximize the therapeutic effect of a subsequently administered nanocarrier or antibody. The global optimization method and TME-normalizing therapy design formulation (introduced in Section 2.5) enable the capability to seek the optimal dose of DEX maximizing the nanocarrier accumulation.

As described in Section 2.5, we considered two cases of TME-normalizing therapy design problems: (Case 1) the relationships between DEX dose and L_p and K are established based on the original data from Martin et al. [10], expressed as (5) and (6); and (Case 2) the relationships between DEX dose and L_p and K are established based on the original data combined with auxiliary data points, expressed as (7) and (8). Both TME-normalizing therapy design problems were solved to global optimality. It took 2.5 h to solve Case 1 and 3.6 h to solve Case 2. The more complicated relationship between DEX dose and hydraulic conductivities in Case 2 resulted in higher complexity and a longer solution time to reach global optimality. Nevertheless, the proposed methodology with a mixed IA/AA approach for the bounding routine was able to locate an optimal solution in hours. Thus, this short computation time demonstrates that the proposed TME-normalizing therapy design methodology is practical for real-world clinical studies. An optimal solution for Case 1 is found at $x^* = 5.30$ mg/kg, and for Case 2 is found at $x^* = 4.41$ mg/kg. The optimal dose found in Case 1 results in 3% higher concentration accumulation than 3 mg/kg DEX treatment and 74% higher than 30 mg/kg DEX treatment. As a result, the TME-normalizing therapy design methods in this work demonstrate that global optimization can be used in a reasonable time window to determine the optimal dose of DEX, which is predicted to perform 3% better than the best dose determined by the experiments.

3.4 | Dexamethasone Dose Affects the Transvascular Convective Transport Size-Dependently

After finding that the optimal dose of DEX treatment maximizing concentration accumulation, we hypothesized that the size of nanocarriers also affects interstitial concentration. We compared vascular permeability experimental data of two nanocarriers with different hydrodynamic diameters (with data from Martin et al. [10]), because unrelated previous studies demonstrated that vascular permeability depends on the nanocarrier size [53,6,7]. The smaller nanocarrier is 13 nm, which is similar to the size of nanoparticle albumin-bound paclitaxel in circulation [7], and the larger is similar to the size of NC-6004, which is a clinical-stage polymeric micelle containing cisplatin [10]. Using this experimental data and our mathematical model, we investigated the model-predicted interstitial concentration with respect to tumor radial position for these nanocarriers. As illustrated in Figure 9(a), the interstitial concentrations for the control case are almost the same for 32 nm and 13 nm dextrans. And for 3mg/kg DEX treatment case illustrated in Figure 9(b), the peak for 13 nm dextran is slightly higher, but the overall concentration distribution is still very close for these dextrans. However, for 30 mg/kg DEX treatment case illustrated in Figure 9(c), the concentration profile for 13 nm dextran is higher than 32 nm. A possible reason is that the vessel wall pore size decreases with 30 mg/kg DEX treatment [10]. Thus, the steric hindrance is larger, especially for larger nanocarriers. Consequently, there are fewer larger nanocarriers that transport into the tumor tissue, leading to a lower concentration profile. To better understand this phenomena, we needed to investigate the effects of convective and diffusive transport.

We quantified the spatially-averaged convective and diffusive fluxes for 13 nm and 32 nm dextrans to demonstrate their impact on accumulation. As illustrated in Figure 9(d), 3 mg/kg DEX treatment enhances convection to a similar extent for each dextran (360% increase for both 13 and 32 nm dextran compared with the control case).

However, 30 mg/kg DEX treatment leads to a 80% increase of convection for 32 nm dextran and a 180% increase for 13 nm dextran. Therefore, the relatively lower convective flux with 30 mg/kg DEX for 32 nm dextran results in less accumulation into the tumor tissue. In addition, we found that DEX reduces diffusion for both nanocarriers. The higher interstitial concentration and smaller pore size with 30 mg/kg DEX lead to lower diffusive fluxes. Since diffusion is inversely related to hydrodynamic diameter of nanocarriers, reduced diffusion after DEX is more important for smaller nanocarriers, which rely on diffusion. In conclusion, we found 3 mg/kg DEX enhanced transvascular transport size-independently, which conforms to the findings using the ECM normalizing agent tranilast in Papageorgis et al.[54]. However, given the antiangiogenic properties of DEX, an excess dose of DEX is less effective for enhancing convection especially for larger nanocarriers.
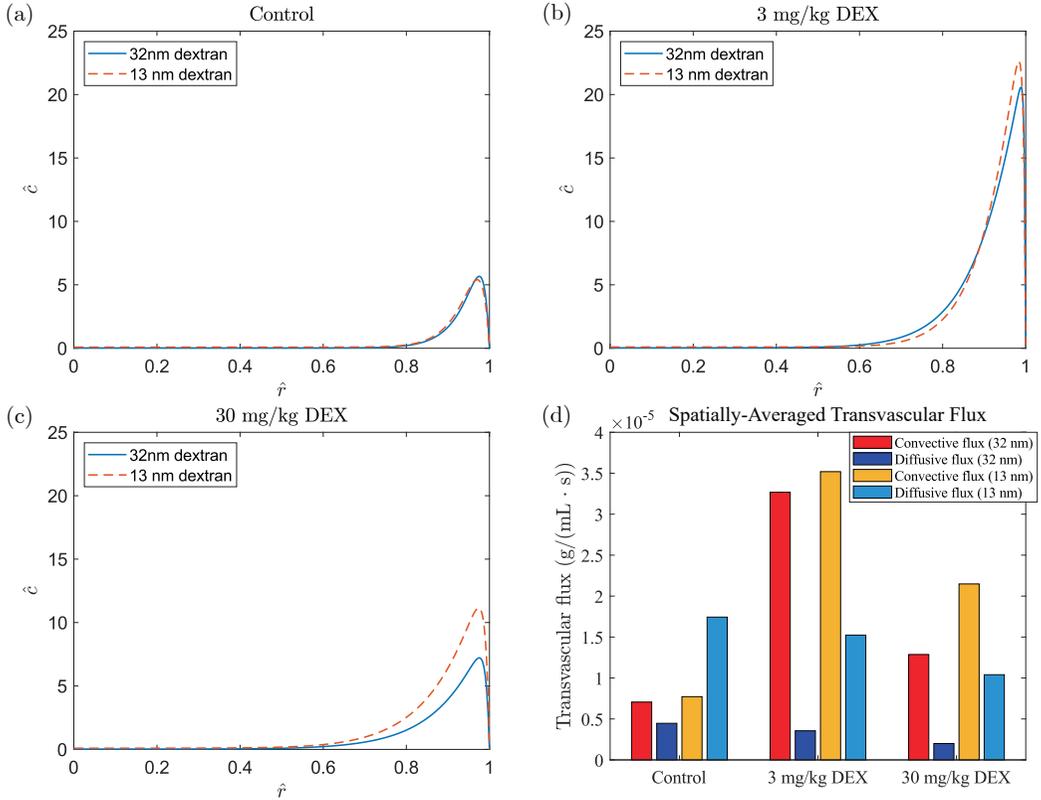

FIGURE 9 Interstitial concentrations $\hat{c}$ of different sizes nanocarriers (500 kDa nanocarrier - 32 nm; 70 kDa nanocarrier - 13nm; Case 1 - 16.40 nm) one-hour post-administration are plotted versus dimensionless tumor radial position $\hat{r}$ for (a) control; (b) 3 mg/kg DEX treatment; and (c) 30 mg/kg DEX treatment cases. (d) The spatially-average transvascular convective and diffusive fluxes are plotted for 32 nm and 13 nm dextrans one-hour post-administration. The interstitial concentration with 30 mg/kg DEX treatment for 32 nm dextran is lower than 13 nm dextran mainly due to its lower convective flux.

3.5 | Global Optimization Determines the Dexamethasone Dose and Nanocarrier Size Maximizing Accumulation

We found that DEX enhances convection yet reduces diffusion, so we sought to determine the optimal hydrodynamic diameter of nanocarrier that exploits the balance of these two effects to realize a maximum accumulation with safety/performance specifications. We considered three cases of drug size design problems. These corresponded to 3 mg/kg DEX treatment, the optimal dose of DEX for Case 1 (5.30 mg/kg), and the optimal dose of DEX for Case 2 (4.41 mg/kg), respectively. The 3 mg/kg dose induced the highest transvascular flux in experiments [10], whereas Case 1 and Case 2 were determined from the corresponding TME-normalizing therapy design problems. These drug size design problems formulated as (10) were solved to global optimality. The optimal solutions found and time costs for each case are summarized in Table 6. Note that the optimal nanocarrier sizes in these designs strictly satisfy the safety/performance requirements to avoid potential side effects and guarantee the effectiveness, which constrain the nanocarrier concentrations in the periphery of tumor normal tissue, as demonstrated in (10). Though smaller nanocarriers diffuse and accumulate inside the tumor interstitial space more quickly, it might violate the safety specifications in these designs. Thus, these optimal solutions account for the drug size design results with requirements. In addition, these problems can be solved in minutes, demonstrating the practicability for real-world applications.

TABLE 6 Optimal solutions and time costs of drug size design problems for the case studies of 3 mg/kg DEX treatment, Case 1, and Case 2 of the therapy design problem.

Case study	3 mg/kg	Case 1	Case 2
Optimal solution (d_m^*, nm)	19.65	16.55	12.51
Time (s)	355	384	120

The simultaneous therapy design approach with ANN models formulated as (12) was also performed with Case 1 and Case 2 studies. An optimal solution for Case 1 was found at $(x^*, d_m^*) = (5.32, 16.40)$ and for Case 2 at $(x^*, d_m^*) = (4.38, 12.41)$. The time costs are 42 s for Case 1 and 350 s for Case 2. However, global optimal solution of (11) with the mechanistic model could not be obtained within a reasonable time limit. We expect that continued research on global bounding methods may be able to accelerate convergence and address this issue in the future. Alternatively, we implemented a multi-start local optimization procedure for problems formulated as (11) and selected the results with the lowest objective function values: $((x^*, d_m^*) = (5.33, 16.54)$ for Case 1 and $(x^*, d_m^*) = (4.36, 12.58)$ for Case 2). We found that the optimal solutions obtained with the ANN models are very close to the best-found local optimal results obtained via the multi-start procedure. Since the ANN models were very accurate surrogates of the mechanistic model, this provides supporting evidence that the local results obtained are close estimates of the global optima. Therefore, these results provide support for the practicability of the ANN models for use in optimal decision-making in cancer therapeutics.

The therapy design methods in this work provide capability to identify optimal dose and drug size for maximizing the improvement in nanocarrier delivery induced by TME-normalizing therapies. One area of future work is to investigate the effects of half-life circulation time on drug delivery. Smaller nanocarriers, which diffuse faster than larger nanocarriers, benefit from having a higher intravascular concentration resulting from longer circulation time. Thus, testing the impacts of different circulation time on concentration accumulation of different size nanocarriers can be a useful future study. In addition, Martin et al. [10] reported that TME normalization increases the perfused vascular density, which is not incorporated in this work. Higher vascular density indicates additional functional perfused vessels, which is beneficial for drug delivery and accumulation in tumor tissue. Thus, we predicted that results for TME-

normalizing therapy will be better if accounting for changing vascular density. Additionally, based on simulations of the model, the variation of vascular density (S/V from 50 to 300) evidently does not affect the nanocarrier concentration profiles. Nevertheless, the impacts of the vascular density require further investigation and integrating this attribute could elucidate more details of the underlying transport mechanisms. While the current work demonstrates the influence of transvascular transport on nanocarrier delivery, investigating how dexamethasone affects interstitial transport could establish a more comprehensive foundation for further enhancing therapy design methods.

4 | CONCLUSION

Rigorous methods of model validations and optimal TME-normalizing dose and nanocarrier size therapy designs were developed. This work was motivated by the need for more rigorous methods for *in silico* model-based decision-making in cancer research. We established and demonstrated the use of a comprehensive theoretical framework for model-based applications in preclinical PKPD research and development . The dynamic optimization problems for this study were formulated as PDE-constrained NLPs and solved to global optimality, providing rigorous solutions for cancer drug delivery studies. An efficient bounding routine using IA/AA and DI approaches and a special bounding rule for the Péclet number in the solute source term were proposed for improving the performance of the global optimization algorithm. In addition, machine learning approaches were utilized to establish a data-driven model via ANNs as surrogate models for the original PDE system. The ANNs were utilized in place of the mechanistic model for solving the parameter estimation problems with a simplified formulation. In particular, based on the global solution values obtained for the hydraulic conductivities, transvascular transport was quantified with respect to convective and diffusive fluxes to elucidate their contributions to the accumulation of anticancer nanocarriers in tumors following TME-normalizing DEX treatment. Moreover, a methodology for optimal TME-normalizing therapy design was proposed to optimize the dose of DEX for enhanced accumulation of anticancer nanocarriers in tumors. The nanocarrier size design method was also proposed to determine an optimal size for patient-specific TMEs with safety/performance specifications. Finally, a simultaneous design formulation was considered to determine an optimal dose of DEX and an optimal nanocarrier size that would lead to maximized accumulation in the tumor interstitium. This work can be extended to robust design problems that account for the impacts of uncertainty that may arise from noisy data or incomplete characterization of a patient's TME.

Acknowledgements

references

1. Jain RK, Stylianopoulos T. Delivering nanomedicine to solid tumors. Nature Reviews Clinical Oncology 2010;7(11):653–664.

2. Jain RK. Antiangiogenesis Strategies Revisited: From starving tumors to alleviating hypoxia. Cancer Cell 2014;26(5):605–622.

3. Martin JD, Cabral H, Stylianopoulos T, Jain RK. Improving cancer immunotherapy using nanomedicines: progress, opportunities and challenges. Nature Reviews Clinical Oncology 2020;17(4):251–266.

4. Martin JD, Seano G, Jain RK. Normalizing function of tumor vessels: progress, opportunities, and challenges. Annual Review of Physiology 2019;81(1):505–534.

5. Martin JD, Miyazaki T, Cabral H. Remodeling tumor microenvironment with nanomedicines. WIREs Nanomedicine and Nanobiotechnology 2021;13(6):e1730.

6. Cabral H, Matsumoto Y, Mizuno K, Chen Q, Murakami M, Kimura M, et al. Accumulation of sub-100 nm polymeric micelles in poorly permeable tumours depends on size. Nature Nanotechnology 2011;6(12):815–823.

7. Chauhan VP, Stylianopoulos T, Martin JD, Popovic Z, Chen O, Kamoun WS, et al. Normalization of tumour blood vessels improves the delivery of nanomedicines in a size-dependent manner. Nature Nanotechnology 2012;7(6):383–388.

8. Stylianopoulos T, Munn LL, Jain RK. Reengineering the physical microenvironment of tumors to improve drug delivery and efficacy: from mathematical modeling to bench to bedside. Trends in Cancer 2018;4(4):292–319.

9. Jain RK, Tong RT, Munn LL. Effect of vascular normalization by antiangiogenic therapy on interstitial hypertension, peritumor edema, and lymphatic metastasis: insights from a mathematical model. Cancer Research 2007;67(6):2729–2735.

10. Martin JD, Panagi M, Wang C, Khan TT, Martin MR, Voutouri C, et al. Dexamethasone increases cisplatin-loaded nanocarrier delivery and efficacy in metastatic breast cancer by normalizing the tumor microenvironment. ACS Nano 2019;13(6):6396–6408.

11. Chauhan VP, Martin JD, Liu H, Lacorre DA, Jain SR, Kozin SV, et al. Angiotensin inhibition enhances drug delivery and potentiates chemotherapy by decompressing tumour blood vessels. Nature Communications 2013;4:2516.

12. Stylianopoulos T, Martin JD, Chauhan VP, Jain SR, Diop-Frimpong B, Bardeesy N, et al. Causes, consequences, and remedies for growth-induced solid stress in murine and human tumors. Proceedings of the National Academy of Sciences 2012;109(38):15101–15108.

13. Socinski MA, Jotte RM, Cappuzzo F, Orlandi F, Stroyakovskiy D, Nogami N, et al. Atezolizumab for first-line treatment of metastatic nonsquamous NSCLC. New England Journal of Medicine 2018;378(24):2288–2301.

14. Murphy JE, Wo JY, Ryan DP, Clark JW, Jiang W, Yeap BY, et al. Total neoadjuvant therapy With FOLFIRINOX in combination with losartan followed by chemoradiotherapy for locally advanced pancreatic cancer. JAMA Oncology 2019;5(7):1020.

15. Chauhan VP, Stylianopoulos T, Boucher Y, Jain RK. Delivery of molecular and nanoscale medicine to tumors: transport barriers and strategies. Annual Review of Chemical and Biomolecular Engineering 2011;2(1):281–298.

16. Baxter LT, Jain RK. Transport of fluid and macromolecules in tumors. I. Role of interstitial pressure and convection. Microvascular Research 1989;37(1):77–104.

17. Baxter LT, Jain RK. Transport of fluid and macromolecules in tumors. II. Role of heterogeneous perfusion and lymphatics. Microvascular Research 1990;40(2):246–263.

18. Baxter LT, Jain RK. Transport of fluid and macromolecules in tumors: III. Role of binding and metabolism. Microvascular Research 1991;41(1):5–23.

19. Baxter LT, Jain RK. Transport of fluid and macromolecules in tumors. IV. A microscopic model of the perivascular distribution. Microvascular Research 1991;41(2):252–272.

20. Deen W. Hindered transport of large molecules in liquid-filled pores. AIChE Journal 1987;33(9):1409–1425.

21. Bungay PM, Brenner H. The motion of a closely-fitting sphere in a fluid-filled tube. International Journal of Multiphase Flow 1973;1(1):25–56.

22. Baish JW, Netti PA, Jain RK. Transmural coupling of fluid flow in microcirculatory network and interstitium in tumors. Microvascular Research 1997;53(2):128–141.

23. Sweeney PW, d'Esposito A, Walker-Samuel S, Shipley RJ. Modelling the transport of fluid through heterogeneous, whole tumours in silico. PLOS Computational Biology 2019;15(6):e1006751.

24. Begoli E, Bhattacharya T, Kusnezov D. The need for uncertainty quantification in machine-assisted medical decision making. Nature Machine Intelligence 2019;1(1):20–23.

25. Deshpande D, Pasipanodya JG, Mpagama SG, Bendet P, Srivastava S, Koeuth T, et al. Levofloxacin pharmacokinetics/pharmacodynamics, dosing, susceptibility breakpoints, and artificial intelligence in the treatment of multidrug-resistant tuberculosis. Clinical Infectious Diseases 2018;67(suppl_3):S293–S302.

26. Nelson SD, Walsh CG, Olsen CA, McLaughlin AJ, LeGrand JR, Schutz N, et al. Demystifying artificial intelligence in pharmacy. American Journal of Health-System Pharmacy 2020;77(19):1556–1570.

27. McBride K, Sundmacher K. Overview of surrogate modeling in chemical process engineering. Chemie Ingenieur Technik 2019;91(3):228–239.

28. Pirdashti M, Curteanu S, Kamangar MH, Hassim MH, Khatami MA. Artificial neural networks: applications in chemical engineering. Reviews in Chemical Engineering 2013;29(4):205–239.

29. Horst R, Tuy H. Global optimization. Springer Berlin Heidelberg; 1996.

30. Wilhelm M, Stuber MD. Easy advanced global optimization (EAGO): an open-source platform for robust and global optimization in Julia. In: AIChE Annual Meeting 2017; Minneapolis, MN, Oct 31, 2017. .

31. Wilhelm ME, Stuber MD. EAGO.jl: easy advanced global optimization in Julia. Optimization Methods and Software 2020;p. 1–26. `https://github.com/PSORLab/EAGO.jl`.

32. Harrison GW. Dynamic models with uncertain parameters. In: Proceedings of the first international conference on mathematical modeling, vol. 1 University of Missouri Rolla; 1977. p. 295–304.

33. Walter W. Differential and integral inequalities, vol. 55. New York, NY: Springer-Verlag; 1970.

34. Neumaier A. Interval Methods for Systems of Equations, vol. 37. Cambridge University Press; 1991.

35. Stolfi J, de Figueiredo LH. An Introduction to Affine Arithmetic. TEMA - Tendências em Matemática Aplicada e Computacional 2003 dec;4(3):297–312.

36. de Figueiredo LH, Stolfi J. Affine Arithmetic: Concepts and Applications. Numerical Algorithms 2004 dec;37(1-4):147–158.

37. Wang C, Stuber MD. Recent advances in bounding transient PDE models with parametric uncertainty. In: AIChE Annual Meeting 2020; 2020. .

38. Scott JK, Barton PI. Bounds on the reachable sets of nonlinear control systems. Automatica 2013;49(1):93–100.

39. Yang X, Scott JK. Efficient reachability bounds for discrete-time nonlinear systems by extending the continuous-time theory of differential inequalities. In: 2018 Annual American Control Conference (ACC) IEEE; 2018. p. 6242–6247.

40. Bezanson J, Edelman A, Karpinski S, Shah VB. Julia: a fresh approach to numerical computing. SIAM Review 2017;59(1):65–98.

41. Rackauckas C, Nie Q. Differentialequations.jl–a performant and feature-rich ecosystem for solving differential equations in julia. Journal of Open Research Software 2017;5(1).

42. Sobol' IM. On the distribution of points in a cube and the approximate evaluation of integrals. USSR Computational Mathematics and Mathematical Physics 1967;7(4):86–112.

43. Bessi L, Rackauckas C, Surrogates.jl. GitHub; 2019. https://github.com/SciML/Surrogates.jl.

44. Innes M, Saba E, Fischer K, Gandhi D, Rudilosso MC, Joy NM, et al. Fashionable modelling with flux. CoRR 2018;abs/1811.01457. https://arxiv.org/abs/1811.01457.

45. Innes M. Flux: Elegant machine learning with Julia. Journal of Open Source Software 2018;3(25):602.

46. Hornik K, Stinchcombe M, White H. Multilayer feedforward networks are universal approximators. Neural Networks 1989;2(5):359–366.

47. Hendrycks D, Gimpel K. Gaussian error linear units (GELUs). arXiv preprint 2016;.

48. Elfwing S, Uchibe E, Doya K. Sigmoid-weighted linear units for neural network function approximation in reinforcement learning. Neural Networks 2018;107:3–11.

49. Han M, Shi Z, Wang W. Modeling dynamic system by recurrent neural network with state variables. In: Advances in Neural Networks - ISNN 2004 Springer Berlin Heidelberg; 2004.p. 200–205.

50. Boucher Y, Jain RK. Microvascular pressure is the principal driving force for interstitial hypertension in solid tumors: implications for vascular collapse. Cancer research 1992;52(18):5110–5114.

51. Dunning I, Huchette J, Lubin M. JuMP: A Modeling Language for Mathematical Optimization. SIAM Review 2017;59(2):295–320.

52. Subbiah V, Grilley-Olson JE, Combest AJ, Sharma N, Tran RH, Bobe I, et al. Phase Ib/II trial of NC-6004 (nanoparticle cisplatin) plus gemcitabine in patients with advanced solid tumors. Clinical Cancer Research 2017;24(1):43–51.

53. Yuan F, Dellian M, Fukumura D, Leunig M, Berk DA, Torchilin VP, et al. Vascular permeability in a human tumor xenograft: molecular size dependence and cutoff size. Cancer Research 1995;55(17):3752–3756.

54. Papageorgis P, Polydorou C, Mpekris F, Voutouri C, Agathokleous E, Kapnissi-Christodoulou CP, et al. Tranilast-induced stress alleviation in solid tumors improves the efficacy of chemo- and nanotherapeutics in a size-independent manner. Scientific Reports 2017;7(1).

Supplementary Information

Chenyu Wang[1] | **Samuel Degnan-Morgenstern[1]** | **John D. Martin[2*]** | **Matthew D. Stuber[1*]**

[1]Process Systems and Operations Research Laboratory, Department of Chemical and Biomolecular Engineering, University of Connecticut, Storrs, CT, 06269-3222, USA

[2]Materia Therapeutics, Las Vegas, NV, 89158, USA

Correspondence
Matthew D. Stuber, University of Connecticut, Storrs, CT, 06269-3222, USA
John D. Martin, Materia Therapeutics Inc., Las Vegas, NV, 89158, USA
Email: stuber@alum.mit.edu (MDS); jdmartin@alum.mit.edu (JDM)

Funding information
National Science Foundation, Award Number: 1932723; University of Connecticut

This document provides the background information and data for the paper: **Optimal Therapy Design With Tumor Microenvironment Normalization**.

S1 | TUMOR TRANSPORT MODEL

The 1-dimensional (1D) tumor transport model proposed by Baxter and Jain [1,2,3,4] is used in this study as a mechanistic foundation for studying transvascular exchange and extravascular transport in tumors. The real vasculature of the tumor is intricate and the cells between regions have large differences [5]. There is a necrotic region at the center of the tumor (i.e., most/all cells are dead). In contrast, the outer region of the tumor contains rapidly dividing cells requiring a large blood supply by abundant active blood vessels. Thus, actual solid tumors are spatially heterogeneous and it may be that some physiological parameters in this model are spatially dependent. In our work, we simplify the tumor microenvironment (TME) to be spatially homogeneous without lymphatics or extravascular bindings, which is helpful for certifying and evaluating the overall role of the interstitial fluid pressure (IFP) on fluid transport and penetration of nanocarriers in a tumor. The blood vessels, cells, extracellular matrix (ECM), and other microscopic structures, as

---

illustrated in Figure S1, are also not considered explicitly in the model because this level of granularity is not important at the length scales we are concerned with in this study. In addition, a main focus of our research is on studying the overall macromolecular solute concentrations in a tumor over a prescribed time horizon. Therefore, we utilize spatial averaging in the data and simulation results, which essentially homogenizes the macroscopic structures. In addition, it is also assumed that the vasculature is distributed continuously over the spatial domain rather than at discrete or localized positions.

S1 .1 | Fluid Transport

The fluid transport in the interstitium of a tumor follows Darcy's law:

$$\mathbf{u} = -K\nabla\mathbf{p}. \tag{S1}$$

Here, $\mathbf{u}$ is the interstitial fluid velocity (IFV) (cm/s), K is the hydraulic conductivity of tumor interstitium (cm^2/mm Hg-sec), and $\mathbf{p}$ is the IFP (mm Hg). We assume axisymmetric flow in the spherical coordinate, and (S1) can be simplified to

$$u = -K\frac{dp}{dr}, \tag{S2}$$

where r is the radial position (cm).

The continuity equation for steady-state incompressible fluid flow in spherical coordinates is given by:

$$\frac{1}{r^2}\frac{d(r^2 u)}{dr} = L_p \frac{S}{V}(p_v - p). \tag{S3}$$

Here, L_p is the hydraulic conductivity of the microvascular wall (cm/mm Hg-sec), S/V is the vascular surface area per unit volume (cm^{-1}), and p_v is the vascular pressure (mm Hg). Substituting (S1) into the continuity equation (S3), the steady-state fluid transport model is given by

$$\frac{1}{r^2}\frac{d}{dr}\left(r^2\frac{dp}{dr}\right) = \frac{\alpha^2}{R^2}(p - p_{ss}), \tag{S4}$$

where

$$\alpha = R\sqrt{\frac{S}{V}\frac{L_p}{K}}$$

is a dimensionless parameter representing the ratio of resistances of the fluid flow in the interstitium to across the vasculature, R is the radius of the spherical tumor (cm), and p_{ss} is the steady-state interstitial pressure where the efflux from the vessels equals the influx (mm Hg), and is equal to p_v in this study.

The boundary conditions consist of a no-flux symmetry condition at the center of the spherical tumor and a

Dirichlet condition at the periphery, respectively, as:

$$\left.\frac{dp}{dr}\right|_{r=0} = 0, \tag{S5}$$

$$p|_{r=R} = p_\infty,$$

where p_∞ denotes the surrounding tissue pressure (mm Hg).

S1.2 | Solute Transport

To describe and characterize the transport mechanism of nanocarriers in tumors, the macromolecular solute transport model is governed by the convection-diffusion equation:

$$\frac{\partial c}{\partial t} + \frac{1}{r^2}\frac{\partial(r^2 uc)}{\partial r} = D\frac{1}{r^2}\frac{\partial}{\partial r}\left(r^2\frac{\partial c}{\partial r}\right) + \phi_s, \tag{S6}$$

where c is the concentration of the solute in the interstitium of the tumor (g/mL), D is the diffusion coefficient (cm^2/sec), and ϕ_s is the distributed source term based on a vessel pore model for transcapillary exchange[6], given by

$$\phi_s = L_p\frac{S}{V}(p_v - p)(1 - \sigma)c_v + P\frac{S}{V}(c_v - c)\frac{Pe}{e^{Pe} - 1} \tag{S7}$$

Here, $Pe = L_p(p_v - p)(1 - \sigma)/P$ is the Péclet number representing the ratio of the rates of convection to diffusion across the vascular wall, σ is the solute reflection coefficient, P is the vascular permeability of the solute through the vascular wall (cm/sec), and c_v is the solute concentration in tissue vessels (g/mL). Since the bolus injection model is applied, the vascular solute concentration decays exponentially with time as $c_v = c_o e^{-t/k_d}$, where c_o is the initial macromolecular solute concentration in the blood (g/mL), and k_d is the half-life circulation time of the nanocarriers (sec).

It is assumed that no macromolecular solutes exist in the tumor before injection, and therefore the initial condition is $c(0, r) = 0$. The boundary conditions are defined as:

$$-D\left.\frac{\partial c}{\partial r}\right|_{r=0} + uc|_{r=0} = 0 \tag{S8}$$

$$c|_{r=R} = c_\infty,$$

where the interstitial concentration satisfies the no-flux condition at the center, is continuous across the tumor periphery, and equals c_∞, representing the concentration (g/mL) in the normal tissue surrounding the tumor.

S1.3 | Pore Theory

We follow the pore theory developed in Bungay and Brenner[7]. The pores of the vessels are assumed to be cylindrical, in this case, we can evaluate the hydraulic conductivity of the tumor vessels L_p, the vascular permeability P, and the

reflection coefficient σ by the pore theory

$$L_p = \frac{\gamma r_o^2}{8\mu L} \tag{S9}$$

$$P = \frac{\gamma H D_o}{L}$$

$$D_o = \frac{k_B T}{6\pi \mu r_m}$$

$$\sigma = 1 - W$$

where γ is the fraction of the surface area occupied by pores, r_o is the pore radius (nm), μ is the blood viscosity (mm Hg-sec), L is the thickness of the vessel wall (μm), D_o is the diffusion coefficient of the nanocarrier in free solution at 37°C given by the Stokes-Einstein relationship, k_B is the Boltzmann constant (1.380648×10^{-23} J/K), T is the temperature of solution (310.15 K), r_m is the particle radius (nm), H and W are respectively diffusive and convective hindrance factors based on the ratio of the particle size over the pore size, which are given in Bungay and Brenner[7]:

$$H = \frac{6\pi \Phi}{K_t}, \tag{S10}$$

$$W = \frac{\Phi(2 - \Phi)K_s}{2K_t},$$

where Φ is the partition coefficient defined as the ratio of the average intrapore concentration to that in the bulk solution at equilibrium. When the interactions between the solutes and pore wall are purely steric, the partition coefficient is taken as $\Phi = (1 - \lambda)^2$, where λ is the ratio of particle size (d_m, nm) to the pore size (d_o, nm). Note that λ should be less than one. The K_t and K_s factors for the convective hindrance term W are defined as

$$K_t = \frac{9}{4}\pi^2 \sqrt{2}(1 - \lambda)^{-5/2}[1 + \sum_{k=1}^{2} \alpha_k(1 - \lambda)^k] + \sum_{k=0}^{4} \alpha_{k+3}\lambda^k \tag{S11}$$

$$K_s = \frac{9}{4}\pi^2 \sqrt{2}(1 - \lambda)^{-5/2}[1 + \sum_{k=1}^{2} \beta_k(1 - \lambda)^k] + \sum_{k=0}^{4} \beta_{k+3}\lambda^k$$

The corresponding coefficients a_k and b_k are listed in Table S1. As indicated by (S9), the vascular permeability P depends on the particle size and vessel wall properties, such as pore size, thickness, charge, and arrangement. Larger particles will result in lower P, and when the particle size is larger than the pore cut-off size, P becomes zero. The vascular hydraulic conductivity L_p relies on the morphology of the wall and the fraction of the wall surface occupied by active pores[8].

S1 .4 | Solution Strategy

The fluid and solute transport models were solved numerically. First, the dimensionless form of the tumor radius, IFP, and solute concentration, were defined as:

$$\hat{r} = \frac{r}{R},$$ (S12)

$$\hat{p} = \frac{p - p_\infty}{p_{ss} - p_\infty},$$

$$\hat{c} = \frac{c - c_\infty}{c_o - c_\infty}.$$

After reformulating the tumor transport model into dimensionless form, the centered finite difference method was used to discretize the spatial domain. The IFP profile is obtained by solving the fluid transport model (S4). As for the solute transport model, the backward difference scheme was employed for discretization of the first partial derivative $\partial c / \partial r$. Then, the explicit Euler method was used to integrate the transient convection-diffusion equation with stepsize set as $h = 15$ s to obtain the medicine concentration profile over the tumor radius.

S2 | SET-VALUED MAPPING APPROACHES

This section introduces some basic set-valued mapping approaches utilized in Section 2.2 of the main manuscript as a compensation.

S2 .1 | Interval Arithmetic and Affine Arithmetic

Interval arithmetic (IA) is an arithmetic performed on intervals according to primitive interval computation rules. The main objective of IA to calculate upper and lower bounds for the range of a function in one or more variables. Readers can navigate to Neumaier [9] for details in IA rules. IA suffers from the *dependency problem* as the different intervals in an equation are treated as entirely independent variables. When some of the intervals depend on each other (e.g., a variable occurs several times in an equation), the combinations of IA operations of the function may significantly overestimate the enclosure of the function.

Affine Arithmetic (AA) can overcome the overestimation induced by the dependency problem of traditional IA. AA keeps track of the dependency between the interval variables throughout the calculations resulting in better interval approximations in most cases [10,11]. In addition, the associated properties for the joint range of the interval variables can be represented as a geometry by AA that reduces overestimation. When implementing none-affine operations, an extra noise term is required to estimate the affine approximations of the non-affine part for each operation. Generally speaking, this results in the elementary operations of AA to be more computationally expensive than standard IA. However, the method proposed in Section 2.2 of the main manuscript will only apply AA for affine operations. As such, non-affine operations and the additional complexity that they introduce, are ignored, resulting in no extra time cost over standard IA.

S2 .2 | Differential Inequalities

Differential Inequalities (DI) is an approach using IA for constructing the componentwise lower and upper bounds on the solution set of a system of ordinary differential equations (ODEs), which is first introduced by Harrison [12]. The DI

methods can be categorized into two types: continuous-time DI and discrete-time DI. In continuous-time DI [13], an auxiliary system of ODE-IVPs is formulated and directly sent to a numerical integrator for constructing the bounds. In contrast, the discrete-time DI introduced by [14] reformulates the system of ODEs into a discrete-time form. Then the bounding rules are applied at each discrete time point. Note that we utilized the discrete-time DI method in this work. In addition, for systems in which additional bounding information is known *a priori*, an interval refinement operator can be applied to the standard DI for further reducing overestimation of the bounding results [15]. This method is also implemented in Section 2.2 of the main manuscript for comparison.

S3 | SIMPLIFICATION OF INEQUALITY CONSTRAINTS

In this section, we demonstrate that the inequality constraints on the superficial IFP in (4) of the main manuscript can be expressed as linear constraints on the optimization variables, L_p and K, such that $K = \zeta L_p$, with $\zeta \in \mathbb{R}$.
First, the dimensonless analytical solution of the fluid transport model [1] (S4) can be derived as:

$$\hat{p} = \left(1 - \frac{\sinh(\hat{r}\alpha)}{\hat{r}\sinh(\alpha)}\right), \tag{S13}$$

where α is given in (S4).
Then, the IFP in the superficial region can be represented as:

$$\hat{p}_{peri} = \left(1 - \frac{\sinh(\hat{r}_{peri}\alpha)}{\hat{r}_{peri}\sinh(\alpha)}\right), \tag{S14}$$

where $\hat{r}_{peri}$ is the dimensionless radius from the center towards the superficial region of a tumor.
Substituting (S14) into the inequality constraints of (4) of the main manuscript results in:

$$\left(1 - \frac{\sinh(\hat{r}_{peri}\alpha)}{\hat{r}_{peri}\sinh(\alpha)}\right) \geq \hat{p}_{peri,\min}, \tag{S15}$$

$$\left(1 - \frac{\sinh(\hat{r}_{peri}\alpha)}{\hat{r}_{peri}\sinh(\alpha)}\right) \leq \hat{p}_{peri,\max}. \tag{S16}$$

If (S15) is active, then the following equality holds:

$$1 - \frac{\sinh(\hat{r}_{peri}\alpha)}{\hat{r}_{peri}\sinh(\alpha)} = \hat{p}_{peri,\min}. \tag{S17}$$

Differentiating (S17) with respect to L_p, yields the following expression:

$$\left(-\frac{\hat{r}_{peri}\sinh(\alpha)\cosh(\hat{r}_{peri}\alpha) - \sinh(\hat{r}_{peri}\alpha)\cosh(\alpha)}{\hat{r}_{peri}\sinh^2(\alpha)}\right)\left(\frac{d\alpha}{dL_p}\right) = 0. \tag{S18}$$

Since $\alpha > 0$ always holds ($L_p > 0$), it can be verified that $\left(-\dfrac{\hat{r}_{peri} \sinh(\alpha) \cosh\left(\hat{r}_{peri}\alpha\right) - \sinh\left(\hat{r}_{peri}\alpha\right)\cosh(\alpha)}{\hat{r}_{peri} \sinh^2(\alpha)} \right) \neq 0$. Therefore, if the constraint is active, then we must have:

$$\frac{d\alpha}{dL_p} = 0 \tag{S19}$$

$$\Rightarrow \frac{d\left(R\sqrt{\frac{SL_p}{VK}} \right)}{dL_p} = 0$$

For this expression to hold, this means that α must be constant with respect to L_p. Since all parameters in α other than L_p and K are constants, K must necessarily be a scalar multiple of L_p.

This gives the following result:

$$K = \zeta L_p, \text{ for some } \zeta \in \mathbb{R} \text{ such that } \hat{p} = \hat{p}_{peri,\min}. \tag{S20}$$

By the same procedure, K must be a scalar multiple of L_p if (S16) is active. Therefore, (S15) and (S16) can be simplified as, respectively:

$$K \leq \zeta_{\max} L_p, \tag{S21}$$

$$K \geq \zeta_{\min} L_p. \tag{S22}$$

The values of $\zeta_{\min}$ and $\zeta_{\max}$ are listed in Table 5 of the main manuscript. The values for $\zeta_{\min}$ are calculated according to the following procedure:

1. Choose two different values of L_p within the interval bounds.
2. Solve the nonlinear equation (S17) with each value of L_p for the corresponding K values.
3. Compute $\zeta_{\min}$ as the slope of the secant line joining the two points on an L_p versus K plot.

The calculation of $\zeta_{\max}$ values follow analogously.

S4 | RELATIONSHIP BETWEEN NANOCARRIER SIZE AND PHYSIOLOGICAL PARAMETERS

There are two physiological parameters directly related to nanocarrier size d_m: diffusion coefficient D and half-life circulation time k_d. The previous experimental results for their correlations are listed in Table S4. Nonlinear regression models are established (power model for D versus d_m; Gaussian model for k_d versus d_m) for these quantities as:

$$f_D(d_m) = 1.981 \times 10^{-6} \cdot d_m^{-1.157} + 2.221 \times 10^{-8}, \tag{S23}$$

$$f_{k_d}(d_m) = 1081 \exp\left(-\left(\frac{d_m + 16.63}{84.82} \right)^2 \right) + 517.4 \exp\left(-\left(\frac{d_m - 65.61}{996.6} \right)^2 \right),$$

where f_D and f_{k_d} represent the values of D and k_d, respectively.
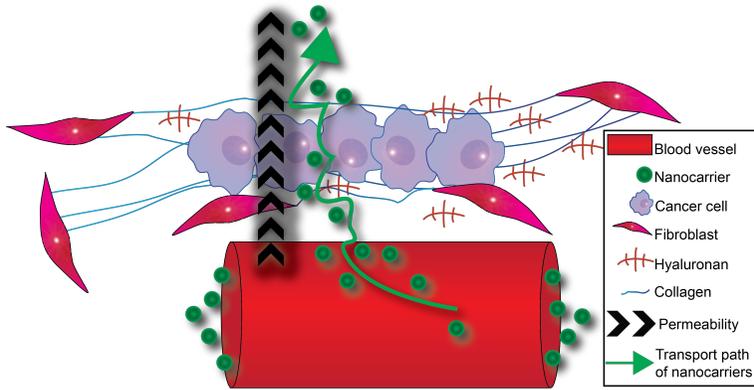
FIGURE S1 A diagram of the tumor microenvironment illustrating fluid and solute transport from the blood vessels to the interstitium with high transvascular permeability[16].
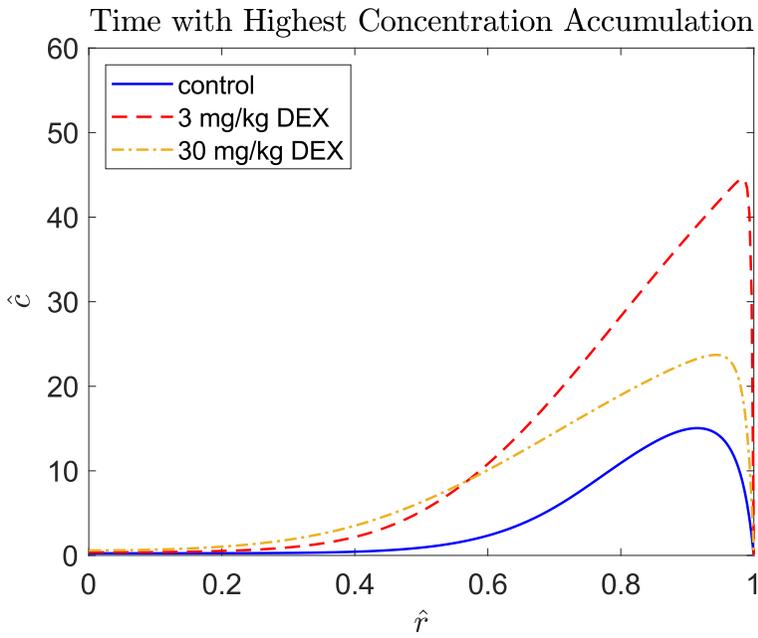
FIGURE S2 The radial interstitial concentration profiles at the time corresponding to the highest spatially-averaged concentrations with respect to control (38.8 h), 3 mg/kg dexamethasone treatment (34.2 h), and 30 mg/kg DEX treatment (53.9 h) cases are presented.
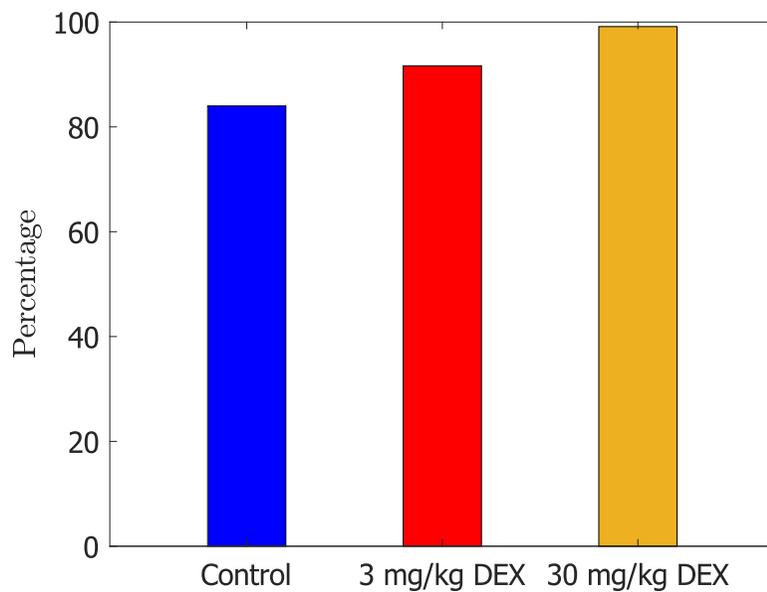
FIGURE S3 The percentages of the spatially-averaged concentrations at 72 h over the respective highest spatially-averaged concentrations for the control, 3 mg/kg and 30 mg/kg dexamethasone (DEX) treatment cases are presented. The DEX treatment enhances the retention effect.
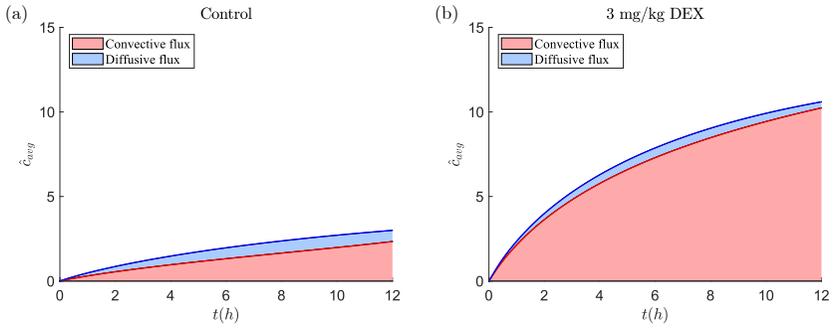
FIGURE S4 The contributions from convective and diffusive flux to spatially-averaged concentrations versus time for (a) control; (b) 3 mg/kg dexamethasone (DEX) treatment cases are presented. The profiles are plotted with a 12-hour horizon because the diffusive flux becomes extremely small after that. The contribution from convective flux becomes more dominant after DEX treatment.
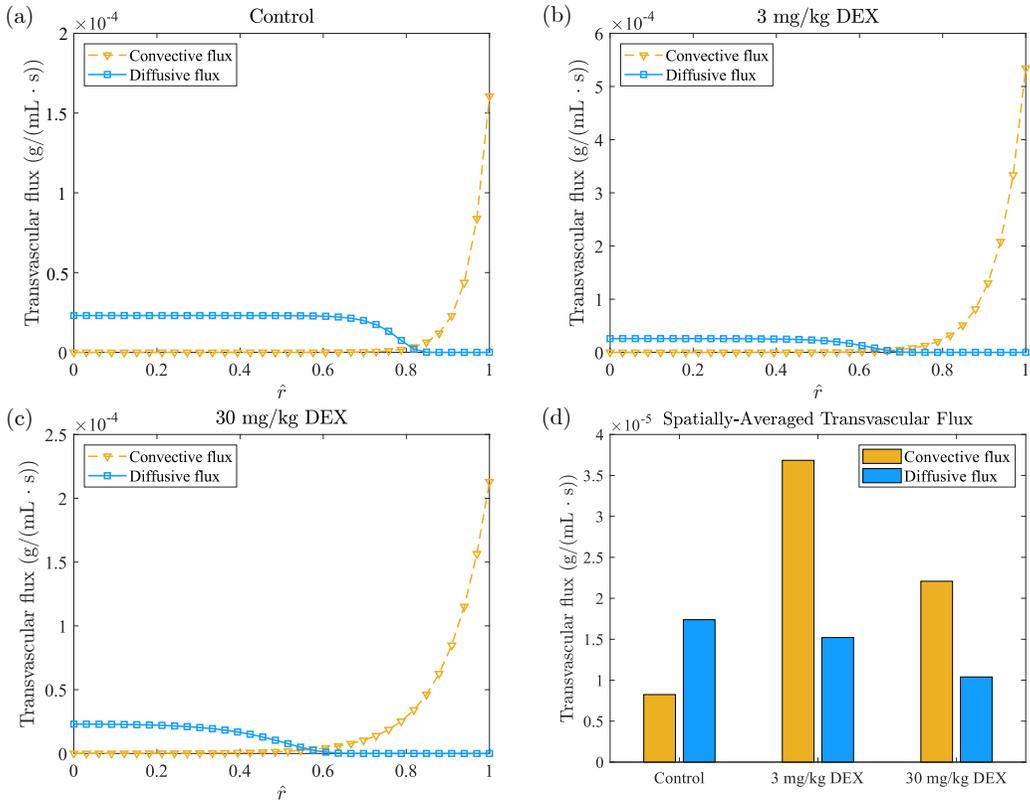
FIGURE S5 The transvascular flux profiles over the dimensionless radius $\hat{r}$ for the (a) control; (b) 3 mg/kg dexamethasone (DEX) treatment; and (c) 30 mg/kg DEX treatment cases with 70 kDa dextran one-hour post-administration are presented. (d) The spatially-averaged convective and diffusive fluxes at one-hour post-administration for different doses of DEX are presented in this bar plot.

TABLE S1 Hydrodynamic coefficients used for the cylindrical pore model. [6]

k	1	2	3	4	5	6	7
α_k	-73/60	77293/50400	-22.5083	-5.6117	-0.3363	-1.216	1.647
β_k	7/60	-2227/50400	4.0180	-3.9788	-1.9215	4.392	5.006

TABLE S2 The bounds on input variables, L_p and K, are used for the surrogate model construction to create ANNs in formulation (3) of the main manuscript.

Bounds	Control		Treatment	
Variable	Lower bound	Upper bound	Lower bound	Upper bound
L_p (cm/mm Hg-sec)	1.00×10^{-7}	1.75×10^{-6}	5.00×10^{-7}	3.50×10^{-6}
K (cm^2/mm Hg-sec)	1.00×10^{-7}	1.00×10^{-6}	7.00×10^{-7}	4.00×10^{-6}

TABLE S3 The benchmark metrics for development time and performance of artificial neural network surrogate models of difference cases (70 kDa - control; 70 kDa - treatment; 500 kDa - control; 500 kDa - treatment) are reported. "70 kDa" and "500 kDa" denote molecular weights of nanocarriers. "Treatment" denotes both 3 mg/kg and 30 mg/kg dexamethasone (DEX) treatment.

	Time Metrics		Performance Metrics	
Case	Data Generation (s)	Training (s)	Mean-Squared Error	Mean-Percent Error (%)
70 kDa - Control	166	473	5.49×10^{-7}	0.339
70 kDa - Treatment	166	538	2.32×10^{-7}	0.102
500 kDa - Control	166	474	3.23×10^{-7}	0.467
500 kDa - Treatment	166	539	1.55×10^{-7}	0.096

TABLE S4 Data for diffusion coefficients [17] and blood half-life circulation time [18] with respect to nanocarrier sizes are reported. These values are used to construct regression models as formulated in (S23).

Particle size	$12nm$	$60nm$	$125nm$	$250nm$
Diffusion coefficient (cm^2/s)	2×10^{-7}	5×10^{-8}	6×10^{-9}	1×10^{-9}
Half-life circulation time (min)	1480	995	582	500*

*represents extrapolation from data

TABLE S5 This table provides benchmark metrics of time and performance (data generation time, training time, mean-squared error and mean-percent error) for ANN surrogate model development in (12) of the main manuscript.

	Time Metrics		Performance Metrics	
	Data Generation (s)	Training (s)	Mean-Squared Error	Mean-Percent Error (%)
$\hat{c}_{avg}^{ANN}$	122	180	7.49×10^{-7}	0.172
$\hat{c}_{peri}^{ANN}$	122	66	5.22×10^{-7}	0.276

TABLE S6 Physiological parameter values are reported for constructing the tumor transport model introduced in Section S1 . "70 kDa" and "500 kDa" denote molecular weights of nanocarriers.

Parameter	Definition	Value	Reference
S/V (cm^{-1})	Vascular density	200	[19]
D (cm^2/sec)	Diffusion coefficient	2×10^{-7} (70 kDa); 1.375×10^{-7} (500 kDa)	[20]
p_v (mm Hg)	Vascular pressure	25	[21]
k_d (min)	Blood circulation time	1480 (70 kDa); 1278 (500 kDa)	[18]
μ (mm Hg-sec)	Blood viscosity	3×10^{-5}	[22]
L (μm)	Vessel wall thickness	5	[23]
γ	Fraction of pore area	1×10^{-3}	[24]

references

1. Baxter LT, Jain RK. Transport of fluid and macromolecules in tumors. I. Role of interstitial pressure and convection. Microvascular Research 1989;37(1):77–104.

2. Baxter LT, Jain RK. Transport of fluid and macromolecules in tumors. II. Role of heterogeneous perfusion and lymphatics. Microvascular Research 1990;40(2):246–263.

3. Baxter LT, Jain RK. Transport of fluid and macromolecules in tumors: III. Role of binding and metabolism. Microvascular Research 1991;41(1):5–23.

4. Baxter LT, Jain RK. Transport of fluid and macromolecules in tumors. IV. A microscopic model of the perivascular distribution. Microvascular Research 1991;41(2):252–272.

5. Nagy J, Chang SH, Shih SC, Dvorak A, Dvorak H. Heterogeneity of the Tumor Vasculature. Seminars in Thrombosis and Hemostasis 2010;36(03):321–331.

6. Deen W. Hindered transport of large molecules in liquid-filled pores. AIChE Journal 1987;33(9):1409–1425.

7. Bungay PM, Brenner H. The motion of a closely-fitting sphere in a fluid-filled tube. International Journal of Multiphase Flow 1973;1(1):25–56.

8. Jain RK, Stylianopoulos T. Delivering nanomedicine to solid tumors. Nature Reviews Clinical Oncology 2010;7(11):653–664.

9. Neumaier A. Interval Methods for Systems of Equations, vol. 37. Cambridge University Press; 1991.

10. Stolfi J, de Figueiredo LH. An Introduction to Affine Arithmetic. TEMA - Tendências em Matemática Aplicada e Computacional 2003 dec;4(3):297–312.

11. de Figueiredo LH, Stolfi J. Affine Arithmetic: Concepts and Applications. Numerical Algorithms 2004 dec;37(1-4):147–158.

12. Harrison GW. Dynamic models with uncertain parameters. In: Proceedings of the first international conference on mathematical modeling, vol. 1 University of Missouri Rolla; 1977. p. 295–304.

13. Walter W. Differential and integral inequalities, vol. 55. New York, NY: Springer-Verlag; 1970.

14. Yang X, Scott JK. Efficient reachability bounds for discrete-time nonlinear systems by extending the continuous-time theory of differential inequalities. In: 2018 Annual American Control Conference (ACC) IEEE; 2018. p. 6242–6247.

15. Scott JK, Barton PI. Bounds on the reachable sets of nonlinear control systems. Automatica 2013;49(1):93–100.

16. Martin JD, Panagi M, Wang C, Khan TT, Martin MR, Voutouri C, et al. Dexamethasone increases cisplatin-loaded nanocarrier delivery and efficacy in metastatic breast cancer by normalizing the tumor microenvironment. ACS Nano 2019;13(6):6396–6408.

17. Pluen A, Boucher Y, Ramanujan S, McKee TD, Gohongi T, di Tomaso E, et al. Role of tumor-host interactions in interstitial diffusion of macromolecules: Cranial vs. subcutaneous tumors. Proceedings of the National Academy of Sciences 2001;98(8):4628–4633.

18. Popović Z, Liu W, Chauhan VP, Lee J, Wong C, Greytak AB, et al. A nanoparticle size series for in vivo fluorescence imaging. Angewandte Chemie 2010;122(46):8831–8834.

19. Yuan F, Leunig M, Huang SK, Berk DA, Papahadjopoulos D, Jain RK. Mirovascular permeability and interstitial penetration of sterically stabilized (stealth) liposomes in a human tumor xenograft. Cancer research 1994;54(13):3352–3356.

20. Pluen A, Boucher Y, Ramanujan S, McKee TD, Gohongi T, di Tomaso E, et al. Role of tumor–host interactions in interstitial diffusion of macromolecules: cranial vs. subcutaneous tumors. Proceedings of the National Academy of Sciences 2001;98(8):4628–4633.

21. Boucher Y, Jain RK. Microvascular pressure is the principal driving force for interstitial hypertension in solid tumors: implications for vascular collapse. Cancer research 1992;52(18):5110–5114.

22. Baish JW, Netti PA, Jain RK. Transmural coupling of fluid flow in microcirculatory network and interstitium in tumors. Microvascular Research 1997;53(2):128–141.

23. Jain RK. Transport of molecules across tumor vasculature. Cancer and Metastasis Reviews 1987;6(4):559–593.

24. Chauhan VP, Stylianopoulos T, Martin JD, Popovic Z, Chen O, Kamoun WS, et al. Normalization of tumour blood vessels improves the delivery of nanomedicines in a size-dependent manner. Nature Nanotechnology 2012;7(6):383–388.